

Aerosol Properties Derived from Aircraft Multi-angle Imaging Over Monterey Bay

Ralph Kahn, Pranab Banerjee, Duncan McDonald

Jet Propulsion Laboratory, California Institute of Technology

4800 Oak Grove Drive, Pasadena CA 91109

For: The Journal of Geophysical Research, Atmospheres
Special Issue on Multi-Angle Measurements and Models

March, 2000

Abstract

The first generic and climatological aerosol retrievals using AirMISR data are presented. Observations in a cloud-free region over Monterey Bay on July 29, 1999, yield complementary generic and climatological results. According to the generic retrieval, the cross-section-weighted, column-mean aerosol properties are: $\tau_a = 0.1 \pm 0.05$, with a preference for values on the low side of the range, $r_a = 0.45 \pm 0.15$, with a preference for the 0.30 to 0.40 sub-range, $n_i < 0.003$, with 0.0 as the most likely value. These properties corresponding to a "large spherical" column-average particle, such as sea salt. The climatological retrieval identifies a Maritime air mass, having a total aerosol optical depth about 0.1, and fractional optical depths for sea salt of 50% in MISR Band 2, and 40% for the sulfate + carbonaceous (medium, spherical) components, to an accuracy of about $\pm 15\%$. These results, in good agreement with nearby surface-based and aircraft observations, represent an early step toward the goal of adding spatial detail and information about temporal variability to the global aerosol climatology with MISR multi-angle data.

1. Introduction

The Multi-angle Imaging SpectroRadiometer (MISR) instrument was launched into polar orbit on December 18, 1999, aboard the Earth Observing System (EOS) Terra spacecraft, after years of preparation and anticipation. MISR is designed to measure upwelling radiance from Earth in 4 spectral bands centered at 446, 558, 672, and 866 nm, at each of 9 emission angles spread out in the forward and aft directions along the flight path at $\pm 70.5^\circ$, $\pm 60.0^\circ$, $\pm 45.6^\circ$, $\pm 26.1^\circ$, and nadir [Diner *et al.*, 1998a]. The spatial sampling rate is 275 meters in the cross-track direction at all angles. Over a period of 7 minutes, as the spacecraft flies overhead, a 360 km wide swath of Earth is successively viewed by each of the cameras. MISR samples a very large range of scattering angles; in mid latitudes, the instrument observes scattering angles between about 60° and 160° . Global coverage is acquired about once in 9 days at the equator; the nominal mission lifetime is 6 years.

The AirMISR aircraft instrument was built in preparation for the flight of MISR [Diner *et al.*, 1998b]. It is intended both to provide data for testing MISR algorithms pre-flight, and as a central part of the long-term MISR calibration and validation program, for the duration of the MISR mission. AirMISR was constructed from a single MISR flight spare camera, and has nearly the same spectral and radiometric characteristics as the MISR cameras [Chrien *et al.*, 1999]. Mounted on a motorized pivot, the AirMISR camera can be pre-programmed to view Earth at emission angles encompassing $\pm 70.5^\circ$ from nadir along the aircraft flight direction. The instrument is designed to fly in the nose of the NASA ER-2 high-altitude aircraft, at an elevation about 20 km above the surface.

For nominal flight conditions, AirMISR samples the surface at 7 m cross-track by 6 m along-track when viewing in the nadir position; the sampling increases to 21 m cross-track by 55 m along-track when viewing at $\pm 70.5^\circ$, the MISR "D camera" angles. A standard AirMISR viewing sequence has the camera dwelling first in the D-forward (Df) MISR viewing position, and then successively stepping through the Cf (60°), Bf (45.6°), Af (26.1°), An (nadir), A-aft (Aa), Ba, Ca, and Da angles during a 13 minute, 156 km ER-2 flight line. This sequence is timed so overlap occurs for all 9 viewing positions over the entire An image, and area 11 km cross-track by 9 km along-track. Since the camera acquires data centered every 8 m on the surface, the samples overlap considerably for the steeper viewing positions. The AirMISR Level 1B2 (L1B2) processing resamples the images for all viewing positions to a uniform grid of 27.5 m pixels (one tenth of a MISR pixel). For a given viewing position, values assigned to each L1B2 pixel are the arithmetic means of all measurements at that viewing angle whose centers fall within the 27.5 m cell.

Engineering checkout flights for AirMISR were completed in the spring of 1999. The first cloud-free, dark water science sequences were acquired on Tuesday, June 29, 1999 over Monterey Bay, California, between 10:30 and 11:05 AM local time. Run 1 trended roughly northward, close to the ground track for the EOS spacecraft; the flight line for Run 2 headed eastward, toward the sun, approximately orthogonal to Run 1. Figure 1 is a map of the Monterey coast, indicating the locations of these flight lines and of the An images for both runs, and Figure 2 is a gray-scale rendition of the An image for Run 1. Table 1 gives the corner locations and timing of the An images.

One of the major science objectives of the MISR program is to derive aerosol physical properties, in addition to optical depth, from multi-angle data. To this end, we developed several research algorithms and explored their sensitivity using simulated MISR data [Kahn *et al.*, 1997; 1998; 2000]. Their performance is expected to be best over dark water, where the surface contribution to the observed radiance is minimal. We use these algorithms, at least initially, with the MISR red and near-infrared (NIR) bands only, where the ocean surface is expected to be darkest.

The generic algorithm [Kahn *et al.*, 1998] interprets top-of-atmosphere radiances in terms of a column-averaged, cross-section-weighted mean effective aerosol population having unimodal, log-normal size distribution and uniform composition. The generic retrieval produces aerosol physical properties with a minimum of assumptions; it is a good way to assess the information content of observations. But the effective column particle properties obtained may not correspond to any particles that are actually observed in the field or predicted by transport models.

An alternative, climatological aerosol retrieval [Kahn *et al.*, 2000], asks how well MISR can distinguish among assumed, climatologically likely, mixtures of pure particle types. Climatological retrievals must assume a climatology of component particles and mixtures. But the additional assumptions allow us to distinguish, as much as possible, air masses containing common mixtures of aerosols in Earth's atmosphere, and to compare retrieval results with *in situ* observations and with aerosol transport model predictions.

The June 29 AirMISR Monterey Bay data provides our first opportunity to exercise the research aerosol retrieval algorithms with real data, which is the subject of this paper. The next sections explain how AirMISR data are processed from L1B2 data numbers (DNs) into band-corrected equivalent reflectances needed for the aerosol retrievals, and how simulated data are generated and compared with the measurements. The following sections present the generic and climatological retrieval results for the Monterey experiment. The final section places these results into a larger context, and presents the conclusions.

2. The AirMISR Data

Level 1 AirMISR geometric, radiometric, and spectral calibration processing follows closely the procedures established for handling MISR data [Bruegge *et al.*, 1999a; 1999b; 1998a; Jovanovic *et al.*, 1996]. The key data products for the current study are the AirMISR L1B2 standard data files for Run 1 and Run 2, 990629_monterey, which are archived in Hierarchical Data Format for EOS (HDF-EOS).

The AirMISR L1B2 images have been corrected for any dropped lines using linear interpolation. Some adjustment is made for airplane roll and pitch errors based on the Global Positioning System (GPS)-derived aircraft navigation file. But, as illustrated in Figure 3a, small changes in aircraft pitch still alter the view zenith angle by several degrees. Figure 3 also illustrates how view azimuth varies by 60° over the AirMISR Aa image. Due to the 704 km elevation and relatively stable spacecraft platform on which MISR flies, variations in viewing geometry over MISR images are orders of magnitude smaller than those for AirMISR.

For AirMISR analysis, we select patches 21 by 21 pixels in size, over which the viewing geometry and radiance patterns are fairly uniform. Two white squares in Figure 2 locate 2 of the 3 main patches used for this study. (The third patch was selected in the Run 2 data.) Also visible in this highly stretched image is a pattern of streaks running parallel to the line of flight. This pattern is more pronounced in the images taken at steeper viewing angles, but it shows up only for low-contrast targets such as the ocean surface, and usually amounts to less than 2% (always less than 5%) differences in reflectance. The MISR and AirMISR cameras each contain 4 line arrays of 1504 active pixels, one line for each color band. An image is built up as the line arrays, which are oriented cross-track, are carried along-track by the motion of the instrument. The streak pattern arises from tiny variations in pixel-to-pixel calibration.

The standard AirMISR L1B2 product includes a band-and-camera specific, pixel-by-pixel Data Quality Indicator (DQI), that is set to 0 for useable data, and to 255 if a flag is set at any step in the Level 1 processing. (For the standard MISR L1B2 product, there are separate radiometric and geometric data quality indicators, each of which can assume values between 0 and 3.) We include only pixels with DQI=0 in the AirMISR analysis. For the selected Monterey experiment data, all pixels meet this criterion.

Table 2 contains the mean and standard deviation values for the view zenith and azimuth, as well as the sun zenith and azimuth, at each of the 9 look angles, for all 3 patches. Viewing down toward Earth, azimuth is measured clockwise from north. In all cases, the geometry varies much less than 1 degree over a patch. The last column gives the sun glint angle, defined as:

$$\text{Sun Glint Angle} = \cos^{-1} \{ \cos(\text{sun zenith}) \times \cos(\text{view zenith}) + \sin(\text{sun zenith}) \times \sin(\text{view zenith}) \times \cos(\text{sun azimuth} - \text{view azimuth}) \} \quad (1)$$

When this angle is small, the camera is looking in a direction near that of the sun's specular reflection, and the data may be contaminated. The size of the region affected by specular reflection depends on surface type, and for ocean, it also depends on wind speed, wind azimuth, and sun position relative to the viewing direction. In the AirMISR observations used here, the standard deviations for data having sun glint angle below 30° or 40° are relatively large, indicating possible contamination; a sun glint mask allows us to eliminate contaminated views from the analysis.

Radiometry data for the 3 patches are given in Table 3. Columns 2 through 5 contain the mean and standard deviation values of the spectral DNs for each look angle and patch, as extracted from the AirMISR L1B2 product. (Note that the "DNs" in the L1B2 product are not the original instrument DNs; they are integer representations of radiometrically calibrated and scaled, geometrically resampled radiances derived by MISR L1B1 and L1B2 processing.) The next 4 columns show the spectral equivalent reflectances, along with estimates of the standard deviation. These are calculated according to:

$$\rho(l,k) = \text{DN}(l,k) \times \text{Rad_scale_factor}(l) \times \pi \times D^2 / \text{std_solar_wgted_height}(l) \quad (2a)$$

$$\sigma_p(l,k) = \Delta \text{DN}(l,k) \times \text{Rad_scale_factor}(l) \times \pi \times D^2 / \text{std_solar_wgted_height}(l) \quad (2b)$$

Here indices l and k are for band and camera, respectively. DN and Δ DN are the L1B2 mean and standard deviation data numbers for the look angle and patch of interest, Rad_scale_factor is a band-specific radiometric scale factor, D is the Earth-sun distance in AU, and std_solar_wgted_height is the band-specific normalization needed to obtain equivalent reflectance. All the factors needed are stored as "Grid Metadata" in the standard AirMISR L1B2 product.

For a solar-spectrum-weighted signal, the AirMISR red band has a 4.92% out-of-band sensitivity, coming primarily from blue light. This is about 2.5 times the out-of-band sensitivity for the spacecraft MISR red band, and nearly twice the out-of-band sensitivity of any other band on either the MISR or AirMISR instruments [Chrien *et al.*, 1999]. The final 4 columns of Table 3 contain band-corrected and ozone-corrected equivalent reflectances. The band correction is calculated separately for each look angle, by multiplying the vector of 4 spectral equivalent reflectances obtained from equation 2a for a given look angle by a correction matrix:

$$[\rho^{\text{corr}}] = [[C]] \times [\rho] \quad (3)$$

The terms in each row of the correction matrix C sum approximately to 1, and the off-diagonal terms are 2 or 3 orders of magnitude smaller than the diagonal terms. The matrix C is given in the Grid Metadata of the AirMISR L1B2 Product, as `spectral_corr_matrix`.

A correction is then made to the equivalent reflectance in each band for absorption by stratospheric ozone. The ozone optical depth is

$$\tau_{\text{ozone}}(l) = c_l D_{\text{ozone}} \quad (4a)$$

where c_l is a band-specific constant, equal to 4.26×10^{-6} , 1.05×10^{-4} , 5.09×10^{-5} and 3.94×10^{-6} for MISR bands 1 to 4, respectively, and D_{ozone} is in Dobsons [Diner *et al.*, 1999a]. The ozone-corrected equivalent reflectance for spacecraft MISR measurements is:

$$\rho(l,k)_{\text{ozone-corrected}} = \rho(l,k) \cdot \exp \left[\tau_{\text{ozone}} \left(\frac{1}{\cos(\text{sun_zenith})} + \frac{1}{\cos(\text{view_zenith})} \right) \right] \quad (4b)$$

Since AirMISR flies below the stratospheric ozone layer, the $\cos(\text{view_zenith})$ term in equation 4b is eliminated, and the correction for AirMISR is independent of view angle. The ozone correction is largest in MISR band 2, but still amounts to no more than half the Rayleigh optical depth in that band, even when the ozone column is as high as 450 Dobsons. We use the band- and ozone-corrected equivalent reflectances in the AirMISR analysis, with an ozone column of 320 Dobsons for the Monterey Bay experiment.

3. Modeling MISR Radiances and Comparing with Observations

This section discussed the tools we use to interpret MISR and AirMISR observations in terms of aerosol characteristics.

3.1. The MISR Simulation Radiative Transfer Model

The MISR Team has developed a radiative transfer code that simulates reflectances as would be observed by MISR for arbitrary choice of aerosol mixture, amount, and vertical distribution, variable surface reflectance properties, and user-selected sun and viewing geometry [Diner *et al.*, 1999b; Martonchik *et al.*, 1998]. It is based on the matrix operator method [Grant and Hunt, 1968]. Radiances for mixtures of aerosol types are obtained by combining radiances for the individual components, weighted by fractional contribution to optical depth, according to the modified linear mixing method of Abdou *et al.* [1997].

For the present study we run the model to simulate MISR measurements over a Fresnel-reflecting ocean surface, in a cloud-free, Rayleigh scattering atmosphere with 1.013 bar surface pressure, a

standard mid-latitude temperature profile, and aerosols (except transported accumulation mode dust) concentrated in a near-surface layer. A correction is made to the MISR band most affected by water vapor, Band 4 (at 865 nm), based on a typical mid-to-low latitude maritime profile [Diner *et al.*, 1999b]. It amounts to a band-averaged absorption optical depth of 0.002, which is small compared even to 0.016, the standard atmosphere Rayleigh scattering optical depth for Band 4, and is negligible compared to anticipated MISR sensitivity to aerosol optical depth, of 0.05 or 20%, whichever is larger [Kahn *et al.*, 1998].

The ocean surface boundary condition models whitecaps and sun glint, using standard approaches that depend on near-surface wind speed. Since we use only MISR red and NIR channels for dark water aerosol retrievals, a third component of ocean surface reflection, arising from underlight, is so small it can be ignored [Wang and Gordon, 1994]. The bi-directional reflectance factor (BRF) for the ocean surface due to whitecaps (in the absence of diffuse skylight) is given by the empirical relationship:

$$R^{whitecap} = 0.22 \times 2.95 \times 10^{-6} \times W^{3.52} \quad (5)$$

where W is the wind speed in m/s, measured 10 meters above the surface. This commonly used relationship combines an equation describing the wind-speed-dependent area covered with whitecaps [Monahan and Muircheartaigh, 1980], with an average albedo of 22% for whitecap patches [Koepke, 1984]. Equation 5 applies at visible wavelengths shorter than about 900 nm, for wind speeds less than about 18 m/sec, and is thought to be accurate to 20 or 30%, depending on unmodeled local conditions [Koepke, 1984]. The result is a wavelength-independent, Lambert contribution to the hemispherical albedo from whitecaps, with values 0.0002, 0.002, and 0.009 for surface wind speeds of 5, 10, and 15 m/s, respectively. For comparison, the standard AVHRR satellite aerosol retrieval algorithm assumes the ocean to be a Lambert surface with hemispherical albedo 0.002 at 670 nm wavelength [Stowe, *et al.*, 1997].

The glitter model is based on the popular semi-empirical relationship between near-surface wind speed (W) and the probable distribution of mean squared ocean surface facet slopes (s^2) of Cox and Munk [1954]:

$$2s^2 = 0.003 + 0.0512 \times W \quad (6)$$

A theoretical ocean surface BRF is obtained by combining equation 6 with the Fresnel reflection equations appropriate to the air-water interface, and with a wave shadowing function derived by Tsang *et al.* [1985]. The result has been applied to a case that includes polarization [Mishchenko and Travis, 1997], and to the scalar situation that accounts only for intensity, as is appropriate to MISR and AirMISR data [Martonchik *et al.*, 1998]. Figure 4 shows the glitter component of the assumed ocean BRF for sun elevation angle 33° , and all view zenith and azimuth angles in the upward-looking hemisphere, for wind speeds of 0, 2.5, 5, and 10 m/s.

3.2. Testing Agreement Between Measurements and Comparison Models

Equivalent reflectances at the MISR angles and bands are generated by the radiative transfer model, for atmospheres containing different aerosol amounts, sizes, shapes, and compositions. The 18 values corresponding to the 9 MISR angles in the red and NIR channels used for ocean aerosol retrievals are then compared to the AirMISR measurements. We define 4 test variables to decide whether a comparison model is consistent with the measurements [Kahn *et al.*, 1998; 2000]. Each is based on the χ^2 statistical formalism [e.g., Bevington and Robinson, 1992].

One test variable weights the contributions from each observed reflectance according to the slant path through the atmosphere of the observation:

$$\chi_{abs}^2 = \frac{1}{N\langle w_k \rangle} \sum_{l=3}^4 \sum_{k=1}^9 \frac{w_k [\rho_{meas}(l,k) - \rho_{comp}(l,k)]^2}{\sigma_{abs}^2(l,k; \rho_{meas})} \quad (7a)$$

where ρ_{meas} is the measured equivalent reflectance and ρ_{comp} is the simulated equivalent reflectance for the comparison model. l and k are the indices for wavelength band and camera, N is the number of measurements included in the calculation, w_k are weights, chosen to be the inverse of the cosine of the emission angle appropriate to each camera k , $\langle w_k \rangle$ is the average of weights for all the measurements included in the summation. $\sigma_{abs}(l,k; \rho_{meas})$ is the absolute calibration uncertainty in equivalent reflectance for MISR band l and camera k . The quantity σ_{abs} varies with equivalent reflectance, and consists of a term due to systematic uncertainty, ϵ_{abs_sys} , that is expressed as a percent in the standard MISR and AirMISR products, and a second term arising from random error, related to the inverse of the signal-to-noise ratio (SNR) [Bruegge *et al.*, 1998b]. The SNR_{am} depends on the “averaging mode,” i.e., the number of MISR or AirMISR pixels averaged together to produce the measured DN’s. (For MISR global observations, the averaging mode is 4x4 pixels. For AirMISR L1B2 data, the number of acquired pixels averaged together to make an image pixel varies with viewing geometry, but since the signal-to-noise ratio is so large, no error is introduced by using the values appropriate to 4x4 averaging.) The equation for the absolute calibration uncertainty is:

$$\sigma_{abs}^2 = \rho_{meas}^2 \left[\left(\epsilon_{abs_sys}(l,k; \rho_{meas}) / 100 \right)^2 + \left(SNR_{am}(l,k; \rho_{meas}) \right)^{-2} \right] \quad (7b)$$

Although ϵ_{abs_sys} can vary with l , k , and ρ_{meas} , the early assessment made of the calibration error budget produced a value of 1.6 for all cases [Bruegge *et al.*, 1998b]. Even for dark water scenes, the AirMISR and MISR cameras exhibit high signal-to-noise ratios. For equivalent reflectances of 0.001, the smallest values found in this study (Table 3), the first term in brackets in equation 7b is still about 2 orders of magnitude larger than the second term. (For this reason, the SNR term was ignored in sensitivity studies based on simulations of MISR data [Kahn *et al.*, 1997; 1998; 2000].) Values of σ_{abs}^2 are of order 10^{-7} for the AirMISR data used here, except for sun glint contaminated pixels, which have values of order 10^{-5} .

χ_{abs}^2 alone reduces 18 measurements to a single statistic. χ_{abs}^2 emphasizes the absolute reflectance, which depends heavily on aerosol optical depth for bright aerosols over a dark surface. However, there is more information in the measurements that we can use to improve the retrieval discrimination ability. A second χ^2 test variable emphasizes the geometric properties of aerosol scattering, which depend heavily upon particle size and shape. Camera-to-camera relative uncertainty is small compared to the absolute uncertainty. The χ_{geom}^2 test variable takes advantage of this fact -- each spectral measurement is divided by the corresponding spectral measurement in the nadir camera:

$$\chi_{geom}^2 = \frac{1}{N\langle w_k \rangle} \sum_{l=3}^4 \sum_{\substack{k=1 \\ k \neq \text{nadir}}}^9 \frac{w_k \left[\frac{\rho_{meas}(l,k)}{\rho_{meas}(l, \text{nadir})} - \frac{\rho_{comp}(l,k)}{\rho_{comp}(l, \text{nadir})} \right]^2}{\sigma_{geom}^2(l,k; \rho_{meas})} \quad (8a)$$

where $\sigma_{geom}^2(l, k; \rho_{meas})$ is the uncertainty in camera-to-camera equivalent reflectance ratio appropriate to camera k , band l , and the equivalent reflectance measured by MISR. The expression for σ_{geom}^2 is derived from the expansion of errors for a ratio of measurements ($\sigma^2(f(x, y)) = (df/dx)^2 \sigma_x^2 + (df/dy)^2 \sigma_y^2$ [e.g., *Bevington and Robinson*, 1992]):

$$\sigma_{geom}^2(l, k; \rho_{meas}) = \frac{\sigma_{cam}^2(l, k; \rho_{meas})}{\rho_{meas}^2(l, nadir)} + \frac{\sigma_{cam}^2(l, nadir; \rho_{meas}) \rho_{meas}^2(l, k)}{\rho_{meas}^4(l, nadir)} \quad (8b)$$

$\sigma_{cam}(l, k; \rho_{meas})$ is the contribution of (band l , camera k) to the camera-to-camera relative calibration reflectance uncertainty, and is given by an expression similar to that for σ_{abs} :

$$\sigma_{cam}^2 = \rho_{meas}^2 \left[\left(\epsilon_{cam_sys}(l, k; \rho_{meas}) / 100 \right)^2 + (SNR_{am}(l, k; \rho_{meas}))^{-2} \right] \quad (8c)$$

where ϵ_{cam_sys} is the uncertainty due to systematic factors in camera-to-camera calibration, expressed as a percent; its value is assessed at 1.4 for all cases, based on the calibration error budget [*Bruegge et al.*, 1998b]. Similarly, we define a spectral χ^2 as:

$$\chi_{spec}^2 = \frac{1}{N \langle w_k \rangle} \sum_{k=1}^9 \frac{w_k \left[\frac{\rho_{meas}(band4, k)}{\rho_{meas}(band3, k)} - \frac{\rho_{comp}(band4, k)}{\rho_{comp}(band3, k)} \right]^2}{\sigma_{spec}^2(l, k; \rho_{meas})} \quad (9a)$$

with

$$\sigma_{spec}^2(l, k; \rho_{meas}) = \frac{\sigma_{band}^2(l, k; \rho_{meas})}{\rho_{meas}^2(band3, k)} + \frac{\sigma_{band}^2(band3, k; \rho_{meas}) \rho_{meas}^2(l, k)}{\rho_{meas}^4(band3, k)} \quad (9b)$$

and $\sigma_{band}(l, k; \rho_{meas})$ as the contribution of (band l , camera k) to the band-to-band relative calibration reflectance uncertainty:

$$\sigma_{band}^2 = \rho_{meas}^2 \left[\left(\epsilon_{band_sys}(l, k; \rho_{meas}) / 100 \right)^2 + (SNR_{am}(l, k; \rho_{meas}))^{-2} \right] \quad (9c)$$

ϵ_{band_sys} is the uncertainty due to systematic factors in band-to-band calibration, expressed as a percent; its value is assessed at 0.7 for all cases, based on the calibration error budget [*Bruegge et al.*, 1998b]. We include a maximum deviation test variable that is the single largest term contributing to χ_{abs}^2 (see equation (7a)):

$$\chi_{max_dev}^2 = \underset{l, k}{Max} \frac{[\rho_{meas}(l, k) - \rho_{comp}(l, k)]^2}{\sigma_{abs}^2(l, k; \rho_{meas})} \quad (10)$$

All the other test variables are averages of up to 18 measurements. $\chi_{max_dev}^2$ makes greatest use of any band-specific or scattering-angle-specific phenomenon, such as a rainbow or a spectral absorption feature, in discriminating between measurements and comparison models.

Lastly, the variable χ^2_{\max} is set equal to the χ^2 test variable having the largest value for a model-measurement comparison. This is the most stringent test for that case, the one that determines whether the comparison model is rejected or accepted as representative of the observations.

The quantities $\epsilon_{\text{abs_sys}}$, $\epsilon_{\text{cam_sys}}$, $\epsilon_{\text{band_sys}}$, and SNR_{am} are stored in the AirMISR L1B2 product, as part of the Grid Metadata. They are called `abs_rad_unc_sys`, `cam_to_cam_rel_unc_sys`, `band_to_band_rel_unc_sys`, and `snr_4x4` (for the 4 x 4 averaging mode), respectively. These quantities are reported for each band and camera, and at 15 equivalent reflectance values, which are listed in a vector called `equiv_reflect`. Although the values of all 3 ϵ variables are independent of band, view angle, and measured equivalent reflectance in the early calibration budget assessment, SNR_{am} must be interpolated to the appropriate equivalent reflectance (ρ_{meas}), as indicated in equations 7 to 10. Subsequent re-calibrations may introduce equivalent reflectance dependency in the ϵ variables as well.

3.3. The Interpretation of Test Variable Results

We have defined 4 dependent variables to be used in comparing measurements with models (χ^2_{abs} , χ^2_{geom} , χ^2_{spec} , and $\chi^2_{\text{max dev}}$). Since each χ^2 variable is normalized to the number of channels used, they are “reduced” χ^2 quantities. Formally, $\chi^2 < 1$ means that the average difference between the measured and comparison quantities is less than the associated measurement error. A value less than or about unity implies that the comparison model is indistinguishable from the measurements. Values larger than about 1 imply that the comparison model is not likely to be consistent with the observations.

However, the formal interpretation of the χ^2 statistic does not strictly apply to the test variables used here, since they are actually the averages of correlated measurements from multiple bands and cameras, though each term contributing to these variables may itself be distributed as χ^2 . We estimate that there are 3 to 4 independent pieces of information in the 18 measurements used for dark water MISR aerosol retrievals in most cases [Kahn *et al.*, 1998]. Also, in the expansion of errors in equations 8b and 9b, we neglected the cross-calibration terms. We have no way to assess them with available data, but they are probably much smaller than the direct terms.

In this analysis of AirMISR data, minimum values of χ^2_{\max} usually fall between 15 and 25, higher than those found in purely theoretical sensitivity studies [Kahn *et al.*, 1997; 1998; 2000]. Since values of σ^2_{abs} are of order 10^{-7} , an average difference of only 0.1% between measured and comparison model equivalent reflectances accounts for the larger χ^2 values.

The sensitivity studies used simulated “measurements,” obtained from the same algorithm that produced the comparison model radiances. However, aerosols contributing to measurements of a natural scene are unlikely to exactly match the discrete selection of component aerosol properties and mixtures that comprise the comparison model spaces. With real data, there are also differences between the measured and comparison model radiance patterns from unmodeled (and unknown) aspects of the environment, such as sub-pixel and pixel-to-pixel variability in atmospheric and surface properties. This raises the effective measurement uncertainty value that should be used in calculating formal χ^2 values. Pixel-to-pixel equivalent reflectance variability alone, for the sun-glint-free, half-kilometer patches used in this study, amounts to 1 to 2% (Table 3).

In future validation work, when we have obtained *in situ* measurements of surface and atmospheric variability on spatial scales small compared to MISR or AirMISR pixels, we will reassess the measurement uncertainties used to evaluate χ^2 test variables. For the present study, we consider models having the smallest χ^2_{max} values. Based on experience from the sensitivity studies, we apply one additional attribute when identifying acceptable solutions: systematic and smooth behavior of test variable values for models in the comparison space as one moves away from a model at a local minimum [Kahn *et al.*, 2000].

4. Generic Aerosol Retrievals

The generic aerosol retrieval determines the range of column-averaged, cross-section-weighted mean effective aerosol populations that produce top-of-atmosphere radiances closest to the MISR or AirMISR measurements, as assessed by the 4 χ^2 test variables [Kahn *et al.*, 1998]. We begin by assuming a spherical, unimodal, log-normal size distribution of particles with uniform composition, and step through comparison models covering ranges of aerosol column optical depth (τ_c), column mean aerosol effective radius (r_c), and column mean real and imaginary indices of refraction (nr_c , ni_c). Table 4 gives the 4-dimensional parameter space of comparison model properties selected.

We ran 9 cases for each patch. The nominal case used the mean equivalent reflectances over the patch (Table 3). To provide a crude assessment of confidence in the solutions, we also ran the algorithm with all the equivalent reflectances set to mean + standard deviation (the “mean +” cases), and to mean - standard deviation (the “mean -” cases). For these 3 sets of equivalent reflectances, we assumed near-surface wind speed for the comparison model space to be 0.0, 2.5, or 5.0 m/s. According to the Monterey Bay Aquarium Research Institute M1 buoy, which operated at the time of the AirMISR flight (Figure 1), near-surface winds in the vicinity of the observed location fell between 5 and 10 knots (about 2.5 to 5.0 m/s), closer to the low end of this range.

Figure 5 is a scatterplot matrix of the generic retrieval results for Run 1, Patch 1 of the June 29 Monterey data, using the mean AirMISR equivalent reflectances and assumed 2.5 m/s near-surface wind speed. Each of the 4 independent comparison model aerosol variables, τ_c , r_c , nr_c , and ni_c , is represented by one row and one column in this figure. Each off-diagonal graph is a scatterplot showing values of two variables for models that meet a χ^2_{max} criterion, when compared with the AirMISR measurements. For a given scatterplot, all values of the two aerosol variables not displayed are included in the search for cases that meet the criterion (i.e., this is a projection of the 4-dimensional space onto 2 dimensions, not a 2-D section of the 4-D space). Different symbols are used for cases that meet several ranges of χ^2_{max} criteria, starting with $\chi^2_{max} < 17.5$. This figure provides both the range of each comparison model variable that meets each criterion, and the correlations among variables that meet the criteria. A tabulation of the key results for all 9 equivalent reflectance and assumed wind speed cases is given in Table 5.

Solutions having the smallest χ^2_{max} values are tightly clustered around $\tau_a = 0.05$, and r_a between 0.35 and 0.40 microns. Loosening the χ^2_{max} criterion slightly expands the range of τ_a to 0.05 to 0.15, and of r_a to 0.30 to 0.60. Cases assuming the highest wind speed scatter a little more around these values (Table 5). The imaginary index of refraction n_i has a preferred value of 0.0, and no values exceed 0.003 except for the high wind speed cases. By assuming more reflection from the surface, high wind speed retrievals drive particle absorption (n_i) to larger values. For the smallest χ^2_{max} cases, n_i is at the high end of the parameter space, between 1.53 and 1.55, but loosening the

criterion slightly produces no significant constraint on n_r , as would be expected based on our generic retrieval sensitivity studies [Kahn *et al.*, 1998].

The area around Run 1 Patch 1 contains the highest quality data of the Monterey experiment. We performed generic retrievals on 3 additional patches in the immediate vicinity of Patch 1, each centered 50 to 60 pixels (about 1.5 km) away, to the east, west, and north. The results for all these additional patches are indistinguishable from those for Patch 1. These results included all 9 look angles.

We also analyzed these patches with the An (nadir) look angle masked out. The An view might be slightly contaminated with sun glint, as indicated by the relatively small sun glint angle (Table 2) and possibly higher reflectance standard deviation (Table 3) for An. With An eliminated, the scatter is slightly larger (equivalent to an increase in the χ^2_{max} criterion of 5 to 7 points), but the results are centered on the same values as the 9-angle analyses. Because of the varying air mass factor, we expect the steepest angles ("C" and "D") to provide the tightest constraints on aerosol properties, so elimination of the An look angle is not expected to have a large effect on the result.

For Run 1 Patch 2, the sun glint angles for the Af, An, and Aa look angles are small enough to be considered for possible sun glint contamination (Table 2). The sun glint angle below which a view is actually contaminated depends on near-surface wind speed and the relative azimuths of the sun, wind, and look angle, some of which are not well known. However, a better indication of sun glint effects is provided by the combination of relatively small sun glint angle and relatively large reflectance variability on kilometer length scales. The standard deviation of equivalent reflectances for the An look angle exceeds those of all other look angles by an order of magnitude or more, and those for Af are about a factor 2 higher than the remaining views (Table 3).

We applied the generic retrieval to the Run 1 Patch 2 data with the An look angle masked out, and we experimented with masking out Af and Aa as well. Regardless of these choices, the scene is always brighter than can be accounted for with the range of particle properties and optical depths in the retrieval parameter space (Table 4). The main difference from Run 1 Patch 1 is that the Ca and Da look angle reflectances are on order 10% brighter in red and NIR channels of Patch 2. For the mean equivalent reflectance and (mean + standard deviation) equivalent reflectance cases, solutions are found for Patch 2 only when the wind speed is assumed to be high, creating an excessively bright surface, and even then, the minimum χ^2_{max} values are 50.3 and 70.9, respectively (Table 5). Results having smaller minimum χ^2_{max} occur only for some of the (mean – standard deviation) cases, when the reflectances themselves are set artificially low.

Run 1 Patch 2, which lies in the eastern part of the study area, may be affected by thin cloud. This would explain the progressive brightening in the eastward direction across Figure 2; discrete clouds east of the AirMISR study region are visible in geo-synchronous satellite (GOES) images taken at about the same time. Generally, cloud particles are larger than the largest in the assumed aerosol parameter space, and if the cloud is cirrus, the particle shape assumed by the generic retrieval becomes an issue as well. Relative to spherical particles, the scattering phase function for a natural size distribution of randomly-oriented cirrus particles is higher for scattering angles between 70° and 115°, and lower for scattering angles between about 130° and 150° (Mishchenko *et al.*, 1996). The Ca and Da cameras, which show high reflectances relative to those for Patch 1, have scattering angles of 110° and 103°, respectively, which is also suggestive of cirrus.

Despite the poor agreement between key aspects of the observations and modeled atmospheres for Run 1 Patch 2, the best matches yield optical depths between 0.10 and 0.20, only slightly higher than the Run 1 Patch 1 case. This may be a meaningful result; in simulations, aerosol retrievals based on multi-angle data favor solutions with the correct optical depths over a wide range of assumed particle properties [Kahn *et al.*, 1998; 2000]. The climatological retrieval, presented in

the next section, offers comparison models covering an expanded range of assumed particle properties.

AirMISR flew directly toward the sun on Run 2; view angles Cf, Bf, Af, An, and possibly Df are contaminated by sun glint, based on the data in Tables 2 and 3. With 4 or 5 view angles contaminated, results are less meaningful than those for Run 1. When the Cf, Bf, Af, and An view angles are masked out, the scene appears bright, and solutions with $\chi^2_{max} < 100$ are found only if the near-surface wind speed is assumed to be high, or the equivalent reflectances are set artificially low (Table 5). Although the minimum χ^2_{max} values for the Run 2 cases are nearly 3 times larger than for Run 1 Patch 1, best solutions produce optical depths between 0.05 and 0.10, and effective radii that also fall within the range obtained for Run 1 Patch 1.

The steep “D” angles that are most effective at constraining atmospheric properties, so when the Df view for Run 2 Patch 1 is masked out, along with Cf, Bf, Af, and An, minimum χ^2_{max} values are lowered dramatically and the solution space expands. Over the 9 cases having different assumed wind speeds and reflectance values, results are obtained covering the range of optical depths ≤ 0.55 , radii ≤ 0.50 , $n_i < 0.045$, and all allowed values of n_i (Table 5). Loss of information at the Df angle reduces retrieval sensitivity to imaginary index of refraction. The higher aerosol optical depth values correlate with higher n_i , as would be expected.

In summary, we identified views showing aerosol, probable cloud contamination, and sun glint in the AirMISR Monterey data. Based on the generic retrieval in the uncontaminated region, $\tau_a = 0.1 \pm 0.05$, with a preference for values on the low side of that range. Retrieved $r_a = 0.45 \pm 0.15$, with a preference for the 0.30 to 0.40 sub-range, $n_i < 0.003$, with 0.0 as the most likely value, and n_i could be anywhere in the range 1.33 to 1.55, with a possible preference for 1.53 to 1.55. These properties correspond most closely to a “large spherical” column-average, cross-section-weighted mean particle, such as sea salt in our climatology (Table 7). A more detailed analysis of the measurements in terms of climatologically likely particle mixtures is given in the next section.

5. Climatological Aerosol Retrievals

The climatological aerosol retrieval asks what ranges of assumed, climatologically likely, external mixtures of component aerosols match the MISR or AirMISR measurements, as assessed by the 4 χ^2 test variables [Kahn *et al.*, 2000]. This approach allows us to distinguish, as much as possible, air masses containing common mixtures of aerosols, to monitor their evolution, and to compare retrieval results with *in situ* observations and with aerosol transport model predictions.

The value of a climatological retrieval rests on the quality of the assumed climatology. Most satellite climatological retrievals currently used assume either one or two aerosol components. We adopt the global aerosol climatology developed in Kahn *et al.* [2000]. It is based on the results of monthly, global aerosol transport models for 6 component aerosols [summarized by Tegen *et al.*, 1997], interpolated to a 1° by 1° grid. From 6 component aerosols, 15 possible combinations of 4 components can be selected. But Kahn *et al.* [2000] found that only 5 combinations are needed to classify the 4 most abundant components in the transport model results. These 5 “mixing groups”, listed in Table 6, form the comparison space we use for the AirMISR climatological retrieval.

We allow each of the 4 components in each mixing group to contribute a fraction of the total optical depth varying from 0 to 1, in steps of 0.05. This creates 1,771 comparison models covering all the fractional combinations of 4 components in a mixing group. To this we add comparison model optical depth in MISR Band 2 (τ_c) as another dimension, ranging from 0 to 1 in 0.05 steps. So the

space of comparison models contains 5 mixing groups, 1,771 fractional combinations per mixing group, at 21 optical depth steps, for a total of 185,955 models.

To complete the comparison models, we must provide, in addition to the mixture component fractions, microphysical properties for each component aerosol in the climatology. This is the most difficult part of the climatology to specify, since aerosol properties vary on many spatial and temporal scales. However, we expect MISR to make about a dozen distinctions over dark water based on particle microphysical properties [Kahn *et al.*, 1998]. So MISR will be insensitive to fine distinctions in component aerosol size or composition, and it is appropriate to start by selecting commonly cited properties of broad particle classes.

Such microphysical properties for the 6 components, plus cirrus, are given in Table 7. Note that in Continental aerosol mixing groups (defined in Table 6), accumulation mode sulfate particles are hydrated to equilibrium at 70% relative humidity, and accumulation mode dust particles are assumed to be in the surface layer. For Maritime aerosol mixing groups, accumulation mode sulfate particles are hydrated to 80% relative humidity, and accumulation mode dust particles are assumed to be in a layer 5 to 10 km above the surface, mixed with a scale height of 10 km. The last column in Table 7 refers to the qualitative classification of components based on MISR sensitivities [Kahn *et al.*, 1998; 2000]; sizes are designated small, medium, or large, and shapes are spherical or randomly-oriented non-spherical. The component microphysical properties assumed in this climatology will be reevaluated in light of retrieval results, and in consideration of any field data available for a site of interest.

As with the generic retrieval, we ran 9 cases for each patch, covering mean and perturbed equivalent reflectances as well as assumed near-surface wind speeds of 0, 2.5, and 5 m/s. Figure 6 is a whisker plot matrix that summarizes the results of the climatological retrieval using mean equivalent reflectances for Run 1, Patch 1 of the AirMISR Monterey flight, and assumed wind speed of 2.5 m/s. Each of the 5 rows of plots corresponds to comparisons made between the AirMISR data and models from one of the 5 mixing groups. The columns correspond to different choices of comparison model optical depth. The horizontal axis for each whisker plot allows 6 positions, for each of the 6 pure particle types in this study. The vertical axis shows the range of fractional optical depth from 0 to 1. There are no more than 4 whiskers in each plot, corresponding to the components of the relevant mixing group. Each whisker indicates the largest and smallest fractional optical depth of that component particle, for any comparison model in the mixing group that meets the criterion $\chi^2_{max} < 25$. Longer whiskers indicate that comparison models meeting this criterion span a wider range of fractional optical depth. Note that correlations among components are not shown in Figure 6. However, an "x" on each whisker indicates the component fractional optical depth for the comparison model in the relevant mixing group with the lowest value of χ^2_{max} .

In Figure 6, only models in mixing group 3 meet the criterion, and then only for $\tau_a = 0.1$. This is a Maritime air mass, and the predominant component is sea salt, the large, spherical, non-absorbing particle in the climatology. It accounts for about 50% of the total optical depth in this retrieval. About 25% to 40% is assigned to sulfate and/or carbonaceous components, which are medium, spherical particles that are non-absorbing and slightly absorbing, respectively. This result supports the sensitivity study conclusion that it would be difficult to distinguish these two components with multi-angle data [Kahn *et al.*, 2000]. The remaining 10% to 25% is attributed to black carbon.

Results for other mixing groups that meet a looser criterion, $\chi^2_{max} < 30$, are all Maritime, having roughly 50% sea salt, 40% sulfate + carbonaceous particles, and 10% of a more absorbing aerosol, either black carbon or accumulation mode dust. Since we expect an accuracy of $\pm 15\%$ to

20% for dark water climatological retrievals, based on sensitivity study results. The climatological retrieval produces a consistent picture within the expected accuracy.

Most of the cases that assume perturbed equivalent reflectances and off-nominal wind speeds give similar results. Total column aerosol optical depths for models meeting the $\chi^2_{max} < 25$ criterion are 0.1, except for a few cases when the equivalent reflectance is set low. For these cases, τ_a falls between 0.15 and 0.20, and the retrieval produces unreasonably large fractions of black carbon (in excess of 70%), a phenomenon also observed in sensitivity studies [Kahn *et al.*, 2000].

We also compare Run 1 Patch 1 observations with the 6 Cirrus mixing groups defined in Table 6. For nominal wind speed and mean reflectances, the models that meet the $\chi^2_{max} < 25$ criterion again produce 50% or more sea salt, up to 40% sulfate; the remaining $10\% \pm 5\%$ is associated with combinations of darker components and/or Cirrus. For these models, $\tau_a = 0.1$, as before.

The climatological retrieval was less successful for Run 1 Patch 2, an area likely to be cloud-contaminated according to the generic retrieval analysis. Minimum values of χ^2_{max} exceed 94 for all mixing groups, and these cases represent a wide range of significantly different (>20%) component fractions. Apparently, no combination of the assumed component aerosols (including the one cirrus model in Table 7) provides a good fit. However, the optical depths for the cases having the lowest χ^2_{max} values are all 0.05 or 0.10. More work needs to be done on the sensitivity of AirMISR and MISR to the properties of thin liquid water and ice clouds, particularly in situations where other instruments are taking coincident cloud data for inter-comparison.

6. Discussion

The generic and climatological retrievals for the July 29, 1999 Monterey AirMISR observations, in the uncontaminated region, give complementary results. The generic retrieval searches a 4-dimensional aerosol comparison space thoroughly, at least for spherical particles in the current implementation. Within the assumed climatology, the climatological retrieval identifies air mass types, made of component aerosols, which match the observations.

Based on the generic retrieval, the cross-section-weighted, column-mean aerosol properties are: $\tau_a = 0.1 \pm 0.05$, with a preference for values on the low side of the range, $r_a = 0.45 \pm 0.15$, with a preference for the 0.30 to 0.40 sub-range, $n_i < 0.003$, with 0.0 as the most likely value. These properties correspond most closely to a "large spherical" column-average particle, such as sea salt in the MISR aerosol climatology.

The climatological retrieval identified a Maritime air mass. To an accuracy of about $\pm 15\%$, the retrieved fractional optical depth of sea salt is 50% in MISR Band 2, and 40% for the sulfate + carbonaceous (medium, spherical) components. In agreement with the generic results, the column optical depth comes to about 0.1.

Some near-coincident data, acquired from other sources, may be compared with the AirMISR results:

- According to general circulation model back-trajectories (HYSPLIT, 1999), the near-surface air at Monterey Bay in the late morning of June 29, 1999 spent at least the previous 5 days over the North Central Pacific Ocean. Higher-level air (300 hPa) originated in the Subtropical East Pacific. Such histories would produce a Maritime air mass, as observed.

- The MISR validation team deployed several instruments at the Marina site, just on shore along the AirMISR Run 2 flight line on June 29 (Figure 1). They report an aerosol optical depth of 0.096 at 519.9 nm, 18:02 UTC, that remained within 10% of that value for the subsequent hour, based on Reagan sun photometer measurements [B. Gaitley, M. Helmlinger, and S. Pilorz, personal communication, 1999]. At 18:05 UTC, data from the team's Multi-Filter Shadowband Radiometer (MFRSR) at the site produced aerosol optical depths of 0.091 at 615.5 nm, and 0.109 at 499.6 nm. These values compare well with the AirMISR results.
- About 45 km south east of the AirMISR An image centers, the University of Washington Twin Otter flew two profiles during the AirMISR Runs. A preliminary report by S. Gasso identifies a marine type aerosol and total column optical depth at 550 nm around 0.08, consistent with the other observations. More detailed composition and size distribution data from this experiment will be forthcoming.

The current MISR aerosol climatology [Kahn *et al.*, 2000], derived from transport model results [Tegen *et al.*, 1997], reports the Carbonaceous + Dusty Maritime mixing group for September through March for the Monterey area. On a monthly average, the expected air mass contains about 10% fractional optical depth of the sea salt component, more than 70% sulfate + carbonaceous components, and the rest is accumulation mode dust. For June and July, the climatology for Monterey identifies the Carbonaceous + Dusty Continental mixing group, which does not contain a significant fraction of sea salt. One of the goals of the MISR mission is to add spatial detail and information about temporal variability to the global aerosol climatology. The analysis of AirMISR data, given in this paper, is an early step toward this goal.

Coincident field measurements are needed to quantify the effect of sub-pixel and pixel-average variability on the measurement uncertainty, and to establish the sensitivity of AirMISR and MISR data to naturally occurring cirrus and liquid water clouds. These are the subjects of continuing work, as is the analysis of MISR data on a global scale.

Acknowledgments. We thank Carol Bruegge, James Conel, David Diner, Barbara Gaitley, Mark Helmlinger, William Ledeboer, Roger Marchand, and Stu Pilorz, all members of the MISR Validation team, for helping provide the AirMISR and MISR field data used in this study. Santiago Gasso and Dean Hegg reported their Monterey aircraft results in advance of publication. We thank Carol Bruegge, David Diner, Barbara Gaitley, Santiago Gasso, Veljko Jovanovic, William Ledeboer, John Martonchik, and Stu Pilorz for valuable discussions on this work. The Monterey Bay Aquarium Research Institute provided wind speed data from their M1 buoy. This research is supported by the EOS-MISR instrument program, and by the Climate and Radiation Research and Analysis Program in the Earth Sciences Division of the National Aeronautics and Space Administration, under R. Curran. This work is performed at the Jet Propulsion Laboratory, California Institute of Technology, under contract with NASA.

References

- Abdou, W.A., J.V. Martonchik, R. Kahn, R. West, and D. Diner, "A modified linear-mixing method for calculating atmospheric path radiances of aerosol mixtures", *J. Geophys. Res.* **102**, 16,883-16,888 1997.
- Bevington, P.R. and D. K. Robinson, Data reduction and error analysis for the physical sciences, Second edition, McGraw-Hill, New York, pp. 328, 1992.

- Bruegge, C.J., N.L. Chrien, and D.J. Diner, MISR Level 1 in-flight radiometric calibration and characterization algorithm theoretical basis, JPL D-13398, Rev. A, 1999a.
- Bruegge, C.J., D.J. Diner, R.P. Korechoff, and M. Lee, MISR Level 1 radiance scaling and conditioning algorithm theoretical basis, JPL D-11507, Rev. E, 1999b.
- Bruegge, C.J., V.G. Duval, N.L. Chrien, R.P. Korechoff, B.J. Gaitley, and E.B. Hochberg, MISR prelaunch instrument calibration and characterization results, IEEE Trans. Geosci. Remt. Sensing 36, 1186-1198, 1998a.
- Bruegge, C.J., N. Chrien, D. Diner, R. Kahn, and J. Martonchik, MISR radiometric uncertainty analyses and their utilization within geophysical retrievals, Metrologia 35, 571-579, 1998b.
- Chrien, N.L., C.J. Bruegge, and B.J. Gaitley, AirMISR laboratory calibration and in-flight performance results, Remt. Sensing of Environ., submitted, 1999.
- Cox, C. and W. Munk, Statistics of the sea surface derived from Sun glitter, J. Mar. Res. 13, 198-227, 1954.
- d'Almeida, G.A., P. Koepke, and E.P. Shettle, Atmospheric Aerosols: Global climatology and radiative characteristics, Deepak Publishing, 1991.
- Diner, J., W. Abdou, T. Ackerman, J. Conel, H. Gordon, R. Kahn, J. Martonchik, S. McMuldroch, S. Paradise, B. Pinty, M. Verstraete, M. Wang, and R. West, MISR Level 2 Aerosol Retrieval Algorithm Theoretical Basis, JPL D11400, Rev. D, 1999a.
- Diner, D.J., W.A. Abdou, H.R. Gordon, R.A. Kahn, Y. Knyazikhin, J.V. Martonchik, D. McDonald, S. MCMuldroch, R. Myneni, and R.A. West, MISR Level 2 ancillary products and datasets algorithm theoretical basis, JPL D-13402, Rev.B, 1999b.
- Diner, D.J., J.C. Beckert, T.H. Reilly, C.J. Bruegge, J.E. Conel, R. Kahn, J.V. Martonchik, T.P. Ackerman, R. Davies, S.A.W. Gerstl, H.R. Gordon, J-P. Muller, R. Myneni, R.J. Sellers, B. Pinty, and M.M. Verstraete, Multiangle Imaging SpectroRadiometer (MISR) description and experiment overview, IEEE Trans. Geosci. Remt. Sensing 36, 1072-1087, 1998a.
- Diner, D.J., L.M. Barge, C.J. Bruegge, T.G. Chrien, J.E. Conel, M.L. Eastwood, J.D. Garcia, M.A. Hernandez, C.G. Kurzweil, W.C. Ledebor, N.D. Pignatano, C.M. Sarture, and B.G. Smith, The Airborne Multi-angle Imaging SpectroRadiometer (AirMISR): Instrument description and first results, IEEE Transact. Geosci. Rmt. Sensing 36, 1339-1349, 1998b.
- Grant, I.P., and G.E. Hunt, Solution of radiative transfer problems using invariant S_n method, Mon. Not. Roy. Astron. Soc. 141, 27-41, 1968.
- Hanel, G., The properties of atmospheric aerosol particles as functions of relative humidity at thermodynamic equilibrium with the surrounding moist air, Adv. Geophys. 19, 73-188, 1976.
- HYSPLIT4 (Hybrid Single-Particle Lagrangian Integrated Trajectory) Model, 1999. Web address: <http://www.arl.noaa.gov/ready/hysplit4.html>, NOAA Air Resources Laboratory, Silver Spring, MD.
- Jovanovic, V.M., M. M. Smyth, J. Zong, R. Ando, and G. W. Bothwell, MISR Photogrammetric Data Reduction for Geophysical Retrievals, IEEE Transact. Geosci. Rmt. Sensing 36, 1290-1301, 1998.

- Kahn, R., P. Banerjee, and D. McDonald, "The Sensitivity of Multiangle Imaging to Natural Mixtures of Aerosols Over Ocean ", J. Geophys. Res., submitted, 2000.
- Kahn, R., P. Banerjee, D. McDonald, and D. Diner, "Sensitivity of Multiangle imaging to Aerosol Optical Depth, and to Pure-Particle Size Distribution and Composition Over Ocean ", J. Geophys. Res. **103**, 32,195-32,213, 1998.
- Kahn, R., R. West, D. McDonald, B. Rheingans, and M.I. Mishchenko, Sensitivity of multiangle remote sensing observations to aerosol sphericity, J. Geophys. Res. **102**, 16861-16870, 1997.
- Koepeke, P., Effective reflectance of oceanic whitecaps, Appl. Opt. **23**, 1816-1824, 1984.
- Martonchik, J.V., D.J. Diner, R. Kahn, M.M. Verstraete, B. Pinty, H.R. Gordon, and T.P. Ackerman, Techniques for the Retrieval of aerosol properties over land and ocean using multiangle imaging, IEEE Trans. Geosci. Remt. Sensing **36**, 1212-1227, 1998.
- Mishchenko, M.I., and L.D. Travis, Satellite retrieval of aerosol properties over the ocean using polarization as well as intensity of reflected sunlight, J. Geophys. Res. **102**, 16,989-17,013, 1997.
- Mishchenko, M.I., L. Travis, R. Kahn, and R. West, "Modeling phase functions for dust-like tropospheric aerosols using a shape mixture of randomly oriented polydisperse spheroids," J. Geophys. Res. **102**, 16, 831-16, 847, 1997.
- Mishchenko, M.I., W.B. Rossow, A. Macke, and A.A. Lacis, "Sensitivity of cirrus cloud albedo, bidirectional reflectance and optical thickness retrieval accuracy to ice particle shape," J. Geophys. Res. **101**, 16, 973-16, 985, 1996.
- Monahan, E.C., and I.O. Muircheartaigh, Optimal power-law description of oceanic whitecap coverage dependence on wind speed, J. Phys. Oceanogr. **10**, 2094-2099, 1980.
- Reid, J.S., P.V. Hobbs, R.J. Ferek, D.R. Blake, J.V. Martins, M.R. Dunlap, and C. Liou, Physical, chemical, and optical properties of regional hazes dominated by smoke in Brazil, J. Geophys. Res. **103**, 32,059-32,080, 1998.
- Shettle, E.P., and R.W. Fenn, Models for the aerosols of the lower atmosphere and the effects of humidity variations on their optical properties, AFGL-TR-79-0214, Air Force Geophysics Laboratory, pp.94, 1979.
- Stowe, L.L., A.M. Ignatov, and R.R. Singh, Development, validation, and potential enhancements to the second-generation operational aerosol product at the National Environmental Satellite, Data, and Information Service of the National Oceanic and Atmospheric Administration, J. Geophys. Res. **102**, 16923-16934, 1997.
- Tegen, I., P. Hollrig, M. Chin, I. Fung, D. Jacob, and J. Penner, Contribution of different aerosol species to the global aerosol extinction optical thickness: Estimates from model results, J. Geophys. Res. **102**, 23,895-23,915, 1997.
- Tsang, L., J.A. Kong, and R.T. Shin, Theory of Microwave Remote Sensing, 613 pp., J. Wiley, New York, 1985.
- Wang, M., and H.R. Gordon, Estimating aerosol optical properties over the oceans with the multiangle imaging spectroradiometer: Some preliminary results, Appl. Opt. **33**, 4042-4057, 1994.

World Climate Programme WCP-112. A Preliminary Cloudless Standard Atmosphere for Radiation Computation. IAMAP (International Association for Meteorology and Atmospheric Physics), Boulder, CA, pp.53, 1984.

Figure Captions

Figure 1. Map of the AirMISR Monterey Bay field site for June 29, 1999. Approximate flight lines for Runs 1 and 2 are indicated with light dashed lines joining the end points, which are marked with open triangles, and labeled with latitude, longitude, and AirMISR crossing time (UTC). The locations of the nadir-looking images for Runs 1 and 2, which also correspond to the maximum overlap region for AirMISR data from all angles, are shown as rectangles along the flight lines. The location of the MISR team's Marina coastal field station is designated with a circle-cross labeled Marina. The Monterey Bay Aquarium Research Institute operational buoy location (36° 45' 11" N. latitude, 122° 1' 11" W. longitude) is indicated with a circle-cross labeled M1.

Figure 2. Gray scale versions of the L1B2 AirMISR An (nadir-looking) images for Monterey Bay, June 29, 1999, Run 1. For this image, the Green AirMISR data was assigned to the blue image plane, the Red AirMISR data was set to green, and the Near-IR data was displayed as red, then the aggregate was reproduced as gray-scale image. The image is highly stretched, and would appear dark and uniform without enhancement. The locations of the 21 by 21 pixel study patches are indicated with white squares. The patch coordinates are given in Table 1.

Figure 3. Viewing geometry of the Aa camera position for Run 1, AirMISR Monterey flight, June 29, 1999. These highly stretched gray scale images show (a) view zenith and (b) view azimuth angles. The zenith angle values are around 25° in the darkest areas, and about 29° in the lightest areas, whereas the azimuth angle ranges over 60°, from values near 40° along the left edge, crossing the 0°/360° line, down to values near 340° along the right edge of the image.

Figure 4. Model bi-directional reflection factors (BRFs) for the component of the ocean surface boundary condition due to glitter, with sun zenith angle 33° and sun azimuth 283°, at near-surface wind speed: (a) 0 meters/sec, (b) 2.5 meters/sec, (c) 5 meters/sec, and (d) 10 meters/sec. Zenith and azimuth angles at the peak of each distribution are given, along with the relative value of the BRF at that point, on a linear scale having value 0 at the base.

Figure 5. Generic aerosol retrieval scatterplot matrix for Run 1, Patch 1, of the AirMISR Monterey flight, June 29, 1999. Each of the 4 independent comparison model aerosol variables, τ_c , r_c , nr_c , ni_c , is represented by one row and one column, labeled "Tau," "Radius," "nr," and "ni," respectively. Note that ni_c is on a logarithmic scale; all others are linear. Each off-diagonal graph is a scatterplot showing values of two variables for comparison models that meet a χ^2_{\max} criterion, when compared with the AirMISR measurements. For a given scatterplot, all values of the two aerosol variables not shown are included in the search for cases that meet the criterion. The figure legend identifies the χ^2_{\max} criterion corresponding to each symbol. Shown here is the case for mean equivalent reflectance values (Table 3), and an assumed near-surface wind speed of 2.5 m/s. Other cases are summarized in Table 5.

Figure 6. Whisker plot matrix summarizing climatological retrieval results using mean equivalent reflectances for Run 1, Patch 1, of the AirMISR Monterey flight, and assumed wind speed of 2.5 m/s. The 5 rows show comparisons between the data and each of the 5 non-cirrus mixing groups in Table 6. Each column contains plots for one choice of comparison model optical depth. The horizontal axis in each plot allows 6 positions for whiskers, one for each component in the climatology (Table 7). The vertical axes indicate the fraction of column optical depth in MISR Band 2 contributed by a particle type. Each plot summarizes the comparisons between the AirMISR data and all 1771 comparison models in one mixing group and optical depth. Whiskers are drawn spanning the upper and lower limits of fractional contribution of each component in the mixing group, for any model that meets the criterion $\chi^2_{\max} < 25$. Fractions of component particle

contributions for the comparison model yielding the smallest value of χ^2_{max} are marked by a "x" on each whisker.

Table 1. AirMISR Nadir Image Corner And Patch Locations

Run 1	Start time:	17:31:12 UTC	
Latitude	Longitude	Image Sample[†] (x)	Image Line[†] (y)
36° 46.56'	-122° 32.22'	587	662
36° 40.56'	-122° 33.9'	534	990
36° 39.54'	-122° 27.96'	937	1079
36° 45.54'	-122° 26.28'	992	749
<hr/>			
Patch Corners:			
Run 1 Patch 1	Upper left	654	875
Run 1 Patch 1	Lower right	674	895
Run 1 Patch 2	Upper left	897	910
Run 1 Patch 2	Lower right	917	930
<hr/>			
Run 2	Start time:	17:55:07 UTC	
Latitude	Longitude	Image Sample[†] (x)	Image Line[†] (y)
36° 45.96'	-122° 31.47'	510	470
36° 39.88'	-122° 32.84'	438	879
36° 38.96'	-122° 26.77'	767	939
36° 45.04'	-122° 25.32'	838	530
<hr/>			
Patch Corners:			
Run 2 Patch 1	Upper left	600	650
Run 2 Patch 1	Lower right	620	670

[†]The L1B2 data are geometrically calibrated and co-registered, so image line and sample numbers correspond to the same geographic locations, within calibration uncertainty, for images from a given Run taken at all look angles.

Table 2. Monterey Bay AirMISR Geometry Data, June 29, 1999*

Look Ang.	Sun Zenith	Sun Azimuth	View Zenith	View Azimuth	Sun Glint Angle
Run 1 Patch 1					
Df	37.32 (0.002)	279.6 (0.004)	72.80 (0.019)	188.1 (0.14)	77.29
Cf	36.86 (0.003)	280.1 (0.004)	61.24 (0.025)	186.4 (0.25)	69.45
Bf	36.62 (0.003)	280.3 (0.005)	47.26 (0.037)	183.9 (0.42)	60.27
Af	36.45 (0.003)	280.5 (0.005)	28.89 (0.090)	178.0 (0.80)	50.05
An	36.27 (0.003)	280.7 (0.005)	6.706 (0.442)	111.3 (0.65)	42.88
Aa	36.11 (0.003)	280.8 (0.005)	25.76 (0.073)	23.94 (0.92)	47.98
Ba	35.93 (0.003)	281.0 (0.005)	44.75 (0.026)	16.85 (0.46)	57.79
Ca	35.70 (0.003)	281.3 (0.005)	59.27 (0.007)	14.09 (0.27)	67.01
Da	35.37 (0.004)	281.6 (0.007)	69.58 (0.031)	12.62 (0.17)	74.05
Run 1 Patch 2					
Df	37.24 (0.004)	279.7 (0.006)	72.64 (0.021)	194.0 (0.15)	73.69
Cf	36.80 (0.003)	280.1 (0.005)	61.22 (0.012)	196.7 (0.25)	63.52

Bf	36.56 (0.003)	280.4 (0.005)	47.39 (0.038)	201.1 (0.42)	51.30
Af	36.38 (0.003)	280.5 (0.005)	29.36 (0.117)	211.5 (0.77)	36.29
An	36.21 (0.003)	280.7 (0.005)	11.56 (0.434)	277.6 (0.20)	24.67
Aa	36.04 (0.003)	280.9 (0.005)	27.70 (0.157)	347.3 (0.78)	34.37
Ba	35.87 (0.003)	281.1 (0.006)	45.56 (0.065)	358.6 (0.43)	48.86
Ca	35.63 (0.003)	281.3 (0.005)	59.61 (0.021)	3.267 (0.263)	61.22
Da	35.29 (0.007)	281.7 (0.009)	69.93 (0.092)	5.859 (0.165)	70.41

Run 2 Patch 1

Df	32.59 (0.003)	284.7 (0.004)	71.71 (0.0273)	280.4 (0.15)	39.25
Cf	32.20 (0.005)	285.1 (0.006)	61.20 (0.0415)	279.3 (0.25)	29.28
Bf	32.20 (0.005)	285.4 (0.005)	46.79 (0.0260)	278.2 (0.43)	15.51
Af	31.77 (0.004)	285.7 (0.005)	27.21 (0.0276)	275.6 (0.88)	6.73
An	31.61 (0.004)	285.9 (0.005)	27.70 (0.4248)	209.3 (3.16)	31.07
Aa	31.44 (0.004)	286.1 (0.005)	25.41 (0.0413)	106.3 (0.95)	56.85

Ba	31.27 (0.004)	286.3 (0.005)	45.03 (0.0201)	103.4 (0.45)	76.27
Ca	31.04 (0.004)	286.6 (0.005)	59.41 (0.0080)	102.3 (0.27)	90.38
Da	30.67 (0.004)	287.1 (0.006)	70.38 (0.0048)	101.7 (0.16)	100.93

* Columns 2 through 5 are averages over 441-pixel patches. Numbers in parentheses are standard deviations. All angles are in degrees.

Table 3. Monterey Bay AirMISR Radiometry Data, June 29, 1999*

Look Angle	Blue DN	Green DN	Red DN	NIR DN	Blue Refl.	Green Refl.	Red Refl.	NIR Refl.	Blue BCR	Green BCR	Red BCR	NIR BCR
Run 1 Patch 1												
Df	2140 (10)	1074 (5)	605 (5)	345 (9)	0.1752 (0.0008)	0.0877 (0.0004)	0.0496 (0.0004)	0.0285 (0.0007)	0.1767 (0.0008)	0.0915 (0.0004)	0.0487 (0.0004)	0.0278 (0.0007)
Cf	1618 (6)	763 (3)	390 (4)	201 (2)	0.1325 (0.0005)	0.0623 (0.0002)	0.0320 (0.0003)	0.0166 (0.0002)	0.1336 (0.0005)	0.0650 (0.0003)	0.0311 (0.0003)	0.0160 (0.0002)
Bf	1329 (6)	609 (2)	286 (2)	141 (1)	0.1088 (0.0005)	0.0497 (0.0002)	0.0235 (0.0002)	0.0116 (0.0001)	0.1098 (0.0005)	0.0519 (0.0002)	0.0226 (0.0002)	0.0112 (0.0001)
Af	1206 (4)	555 (4)	261 (4)	133 (4)	0.0987 (0.0003)	0.0453 (0.0003)	0.0214 (0.0003)	0.0110 (0.0003)	0.0996 (0.0003)	0.0473 (0.0003)	0.0206 (0.0003)	0.0106 (0.0003)
An	1181 (8)	555 (7)	272 (7)	151 (7)	0.0967 (0.0007)	0.0453 (0.0006)	0.0223 (0.0006)	0.0125 (0.0006)	0.0975 (0.0007)	0.0473 (0.0006)	0.0216 (0.0006)	0.0121 (0.0006)
Aa	1188 (5)	541 (3)	251 (2)	127 (2)	0.0973 (0.0004)	0.0442 (0.0002)	0.0206 (0.0002)	0.0105 (0.0002)	0.0981 (0.0004)	0.0461 (0.0003)	0.0198 (0.0002)	0.0101 (0.0002)
Ba	1283 (6)	581 (3)	269 (2)	130 (1)	0.1050 (0.0005)	0.0474 (0.0002)	0.0221 (0.0002)	0.0107 (0.0001)	0.1060 (0.0005)	0.0495 (0.0003)	0.0212 (0.0002)	0.0103 (0.0001)
Ca	1552 (5)	707 (4)	348 (3)	171 (2)	0.1270 (0.0004)	0.0577 (0.0003)	0.0286 (0.0002)	0.0141 (0.0002)	0.1282 (0.0004)	0.0602 (0.0003)	0.0276 (0.0002)	0.0136 (0.0002)
Da	1999 (10)	949 (5)	509 (4)	260 (3)	0.1636 (0.0008)	0.0775 (0.0004)	0.0418 (0.0003)	0.0215 (0.0002)	0.1651 (0.0008)	0.0808 (0.0004)	0.0407 (0.0003)	0.0208 (0.0002)
Run 1 Patch 2												
Df	2087 (8)	1072 (8)	628 (6)	347 (4)	0.1708 (0.0007)	0.0875 (0.0007)	0.0515 (0.0005)	0.0287 (0.0003)	0.1723 (0.0007)	0.0914 (0.0007)	0.0507 (0.0005)	0.0279 (0.0003)
Cf	1590 (6)	754 (2)	385 (2)	207 (1)	0.1302 (0.0005)	0.0616 (0.0002)	0.0316 (0.0002)	0.0171 (0.0001)	0.1313 (0.0005)	0.0642 (0.0002)	0.0307 (0.0002)	0.0165 (0.0001)

Bf	1273 (5)	586 (2)	280 (3)	145 (1)	0.1042 (0.0004)	0.0479 (0.0002)	0.0230 (0.0002)	0.0120 (0.0001)	0.1052 (0.0004)	0.0499 (0.0002)	0.0222 (0.0002)	0.0115 (0.0001)
Af	1119 (8)	523 (8)	255 (8)	143 (8)	0.0916 (0.0007)	0.0427 (0.0007)	0.0209 (0.0007)	0.0118 (0.0007)	0.0924 (0.0007)	0.0446 (0.0007)	0.0202 (0.0007)	0.0114 (0.0007)
An	1249 (70)	742 (86)	508 (95)	422 (104)	0.1022 (0.0057)	0.0606 (0.0070)	0.0417 (0.0078)	0.0349 (0.0086)	0.1030 (0.0057)	0.0632 (0.0070)	0.0416 (0.0078)	0.0346 (0.0086)
Aa	1094 (5)	508 (3)	241 (3)	131 (3)	0.0896 (0.0004)	0.0415 (0.0002)	0.0198 (0.0002)	0.0108 (0.0002)	0.0904 (0.0004)	0.0433 (0.0003)	0.0191 (0.0002)	0.0104 (0.0002)
Ba	1241 (5)	570 (3)	270 (3)	137 (1)	0.1016 (0.0004)	0.0465 (0.0002)	0.0222 (0.0002)	0.0113 (0.0001)	0.1025 (0.0004)	0.0485 (0.0003)	0.0213 (0.0002)	0.0109 (0.0001)
Ca	1554 (6)	729 (3)	369 (4)	190 (2)	0.1272 (0.0005)	0.0595 (0.0002)	0.0303 (0.0003)	0.0157 (0.0002)	0.1283 (0.0005)	0.0621 (0.0003)	0.0294 (0.0003)	0.0151 (0.0002)
Da	2070 (12)	1017 (10)	561 (8)	301 (5)	0.1695 (0.0010)	0.0831 (0.0008)	0.0460 (0.0007)	0.0249 (0.0004)	0.1709 (0.0010)	0.0866 (0.0009)	0.0450 (0.0007)	0.0241 (0.0004)
	Run	2	Patch	1								
Df	2280 (10)	1330 (11)	891 (15)	636 (17)	0.1866 (0.0008)	0.1085 (0.0009)	0.0730 (0.0012)	0.0525 (0.0014)	0.1880 (0.0008)	0.1129 (0.0009)	0.0726 (0.0013)	0.0519 (0.0014)
Cf	1709 (34)	1018 (45)	708 (56)	569 (59)	0.1399 (0.0028)	0.0830 (0.0037)	0.0580 (0.0046)	0.0470 (0.0049)	0.1409 (0.0028)	0.0864 (0.0038)	0.0578 (0.0047)	0.0466 (0.0049)
Bf	2062 (168)	1767 (208)	1611 (224)	1586 (246)	0.1688 (0.0138)	0.1441 (0.0170)	0.1320 (0.0184)	0.1310 (0.0203)	0.1694 (0.0137)	0.1499 (0.0176)	0.1339 (0.0188)	0.1310 (0.0204)
Af	2890 (247)	2862 (296)	2864 (327)	2952 (327)	0.2366 (0.0202)	0.2334 (0.0241)	0.2347 (0.0268)	0.2438 (0.0293)	0.2370 (0.0202)	0.2427 (0.0251)	0.2391 (0.0274)	0.2443 (0.0294)
An	1252 (40)	657 (48)	389 (54)	282 (58)	0.1025 (0.0033)	0.0536 (0.0039)	0.0319 (0.0044)	0.0233 (0.0048)	0.1033 (0.0033)	0.0558 (0.0041)	0.0314 (0.0045)	0.0229 (0.0048)
Aa	1434 (3)	653 (4)	314 (4)	153 (3)	0.1174 (0.0002)	0.0533 (0.0003)	0.0257 (0.0003)	0.0126 (0.0002)	0.1184 (0.0002)	0.0554 (0.0003)	0.0248 (0.0003)	0.0121 (0.0002)

Ba	1751 (4)	797 (4)	401 (4)	195 (2)	0.1433 (0.0003)	0.0650 (0.0003)	0.0329 (0.0003)	0.0161 (0.0002)	0.1446 (0.0003)	0.0676 (0.0003)	0.0317 (0.0003)	0.0155 (0.0002)
Ca	2168 (6)	990 (5)	517 (4)	247 (3)	0.1775 (0.0005)	0.0807 (0.0004)	0.0424 (0.0003)	0.0204 (0.0002)	0.1790 (0.0005)	0.0840 (0.0004)	0.1411 (0.0003)	0.0196 (0.0002)
Da	2782 (7)	1316 (4)	732 (5)	357 (4)	0.2277 (0.0006)	0.1073 (0.0003)	0.0600 (0.0004)	0.0295 (0.0003)	0.2297 (0.0006)	0.1116 (0.0003)	0.0585 (0.0004)	0.0285 (0.0003)

*These data are averaged values over 441-pixel patches. Numbers in parentheses are standard deviations. The spectral equivalent reflectances and reflectance standard deviations (columns 6 through 9) are obtained from DNs according to equation 2. Band- and ozone-corrected equivalent reflectances (BCR, columns 10 through 13) are calculated using equations 3 and 4. The band-specific radiometric scale factors (Rad_scale_factor) used for this case: 0.04720 (blue), 0.04653 (green), 0.03853 (red), and 0.02467 (NIR). The band-specific normalizations needed to calculate equivalent reflectance (std_inband_solar_wgtd_height) used: 1872.20430 (blue), 1850.03590 (green), 1524.45570 (red), and 969.84381 (NIR). The Earth-sun distance is 1.016607 for June 29, 1999, and the ozone correction applied here is for a column abundance of 320 Dobsons.

Table 4. The Parameter Space of Comparison Model Properties Used for the Generic Retrieval

	Minimum Value	Maximum Value	# Divisions
Aerosol optical depth at 0.55 microns	0.00	1.00	21
Characteristic Radius	0.05	2.00	40
Real Index of Refraction	1.33	1.55	12
Imaginary Index of Refraction *	0.0	0.50	20

*Logarithmic Scale used.

Table 5. Generic Retrieval Results, Monterey Bay[†]

Case	Wnd Spd (m/s)	Lowest χ^2_{\max}	For	Lowest	χ^2_{\max}	n_i	$\chi^2_m < 22$				$\chi^2_{\max} < 25$				n_i
			τ_a	r_a	n_r		τ_a	r_a	n	n_i	τ_a	r_a	n_r		
Run 1 Patch 1															
Mean	0.0	15.2	0.05	0.40	1.53	0.0	0.05	0.35 - 0.45	1.53 - 1.55	0.0	0.05 - 0.10	0.35 - 0.65	*	0.00 - 0.003	
Mean	2.5	15.4	0.05	0.40	1.53	0.0	0.05 - 0.10	0.35 - 0.60	1.53 - 1.55	0.0 - 0.002	0.05 - 0.10	0.35 - 0.60	*	0.00 - 0.002	
Mean	5.0	19.0	0.05	0.45	1.53	0.0	0.05 - 0.15	0.35 - 0.45	--	0.00 - 0.002	0.05 - 0.15	0.35 - 0.50	*	0.00 - 0.016	
Mean +	0.0	20.5	0.05	0.35	1.55	0.0	0.05	0.35	1.55	0.0	0.05	0.35 - 0.40	1.55	0.00	
Mean +	2.5	18.4	0.05	0.35	1.55	0.0	0.05	0.35	1.55	0.0	0.05	0.35 - 0.40	1.55	0.0	
Mean +	5.0	22.6	0.05	0.45	1.55	0.0	--	--	--	--	0.05	0.35 - 0.45	1.55	0.0	
Mean -	0.0	12.4	0.05	0.40	1.53	0.0	0.05 - 0.10	0.30 - 0.60	*	0.0 - 0.004	0.05 - 0.15	0.30 - 0.60	*	0.0 - 0.004	
Mean -	2.5	14.1	0.05	0.40	1.53	0.0	0.05 - 0.10	0.30 - 0.60	*	0.0 - 0.003	0.05 - 0.10	0.30 - 0.60	*	0.0 - 0.004	
Mean -	5.0	15.7	0.05	0.50	1.55	0.0	0.05 - 0.20	0.25 - 0.50	*	0.0 - 0.022	0.05 - 0.20	0.25 - 0.55	*	0.0 - 0.022	
Run 1 Patch 2 With An masked out															
Mean	0.0	--	--	--	--	--	--	--	--	--	--	--	--	--	
Mean	2.5	--	--	--	--	--	--	--	--	--	--	--	--	--	
Mean	5.0	50.3	0.15	0.10	1.33	0.063	--	--	--	--	--	--	--	--	

Mean +	0.0	--	--	--	--	--	--	--	--	--	--	--	--	--
Mean +	2.5	--	--	--	--	--	--	--	--	--	--	--	--	--
Mean +	5.0	70.9	0.15	0.10	1.33	0.045	--	--	--	--	--	--	--	--
Mean -	0.0	--	--	--	--	--	--	--	--	--	--	--	--	--
Mean -	2.5	19.8	0.10	0.45	1.33	0.001	0.10	0.25 – 0.50	*	0.0 – 0.003	0.10	0.25 – 0.50	*	0.0 – 0.003
Mean -	5.0	--	--	--	--	--	--	--	--	--	--	--	--	--

Run 2 Patch	1	With	Cf,	Bf,	Af, and	An	masked	out						
Mean	0.0	--	--	--	--	--	--	--	--	--	--	--	--	--
Mean	2.5	--	--	--	--	--	--	--	--	--	--	--	--	--
Mean	5.0	47.6	0.05	0.35	1.49	0.0	--	--	--	--	--	--	--	--
Mean +	0.0	--	--	--	--	--	--	--	--	--	--	--	--	--
Mean +	2.5	--	--	--	--	--	--	--	--	--	--	--	--	--
Mean +	5.0	69.0	0.05	0.30	1.49	0.0	--	--	--	--	--	--	--	--
Mean -	0.0	--	--	--	--	--	--	--	--	--	--	--	--	--
Mean -	2.5	86.6	0.10	0.60	*	0.006	--	--	--	--	--	--	--	--
Mean -	5.0	71.7	0.10	0.50	1.45	0.0	--	--	--	--	--	--	--	--

Run 2 Patch	1	With	Df,	Cf,	Bf,	Af	and	An	masked	out				
Mean	0.0	41.1	0.55	0.25	1.33	0.045	--	--	--	--	--	--	--	--
Mean	2.5	13.9	0.45	0.25	1.33	0.032	0.30 - 0.45	0.25 – 0.35	*	0.016– 0.032	0.30 - 0.45	0.25 – 0.35	*	0.016– 0.032
Mean	5.0	47.6	0.05	0.35	1.49	0.0	--	--	--	--	--	--	--	--

Mean +	0.0	--	--	--	--	--	--	--	--	--	--	--	--	--
Mean +	2.5	--	--	--	--	--	--	--	--	--	--	--	--	--
Mean +	5.0	8.6	0.35	0.25	*	0.022	0.20 – 0.45	0.05 – 0.35	*	0.006– 0.045	0.05 – 0.45	0.05 – 0.35	*	0.0 – 0.045
Mean -	0.0	6.6	0.35	0.25	*	0.022	0.30 – 0.45	0.20 – 0.30	*	0.022	0.30 – 0.45	0.20 – 0.35	*	0.011– 0.032
Mean -	2.5	11.0	0.35	0.20	*	0.022	0.25 – 0.40	0.15 – 0.35	*	0.008– 0.032	0.15 – 0.40	0.15 – 0.50	*	0.008– 0.032
Mean -	5.0	42.8	0.35	0.05	*	0.126	--	--	--	--	--	--	--	--

[†] “Case” indicates whether the retrieval was performed on the mean equivalent reflectance values, the (mean + standard deviation) values, or the (mean – standard deviation) values (Table 3). “Wnd. Spd.” is the assumed near-surface wind speed. Columns 4 through 7 are retrieved aerosol properties at the lowest χ^2_{max} value, columns 8 through 11 are the ranges of retrieved aerosol properties for $\chi^2_{max} < 22.5$, and columns 12 through 15 are the ranges of retrieved aerosol properties for $\chi^2_{max} < 25$. In columns 8 through 15, “--” indicates that no solutions were found, whereas “*” indicates that solutions meeting the criterion covered the entire range within the parameter space (Table 4). In columns 3 through 7, “--” means there are no solutions having $\chi^2_{max} < 80$.

Table 6. Climatological Mixing Groups[†]

Mixing Group	Classification	Component 1	Component 2	Component 3	Component 4
1	Carbonaceous + Dusty Maritime	Sulfate	Sea Salt	Carbonaceous	Accum. Dust
2	Dusty Maritime + Coarse Dust	Sulfate	Sea Salt	Accum. Dust	Coarse Dust
3	Carbonaceous + Black Carbon Maritime	Sulfate	Sea Salt	Carbonaceous	Black Carbon
4	Carbonaceous + Dusty Continental	Sulfate	Accum. Dust	Coarse Dust	Carbonaceous
5	Carbonaceous + Black Carbon Continental	Sulfate	Accum. Dust	Carbonaceous	Black Carbon
1C	Cirrus + Carbonaceous Maritime	Sulfate	Sea Salt	Carbonaceous	Cirrus
2C	Cirrus + Dusty Maritime	Sulfate	Sea Salt	Accum. Dust	Cirrus
3C	Cirrus + Black Carbon Maritime	Sulfate	Sea Salt	Black Carbon	Cirrus
4C	Cirrus + Carbonaceous Continental	Sulfate	Accum. Dust	Carbonaceous	Cirrus
5C	Cirrus + Dusty Continental	Sulfate	Accum. Dust	Coarse Dust	Cirrus
6C	Cirrus + Black Carbon Continental	Sulfate	Accum. Dust	Black Carbon	Cirrus

[†] "Accum. Dust" stands for accumulation mode dust. This table is abstracted from Tables 2 and 4 of *Kahn et al.* [1999].

Table 7. Pure Particle Types Assumed for Climatology*

Aerosol Type	r_1 (μm)	r_2 (μm)	r_c (μm)	σ	n_r (MISR band)	n_i (MISR band)	ω_0 (670 nm)	RH (%)	Particle Size/Shape Category
Sulfate (Accum.) over Land	(0.007) 0.007	(0.7) 0.81	(0.07) 0.08	(1.86) 1.88	(1.53) 1.46	0.0 (all)	1.0	(0) 70	Medium Spherical
Sulfate (Accum.) over Ocean	(0.007) 0.008	(0.7) 1.05	(0.07) 0.10	(1.86) 1.87	(1.53) 1.39	0.0 (all)	1.0	(0) 80	Medium Spherical
Sea Salt (Accum.)	(0.05) 0.098	(1.0) 1.98	(0.35) 0.61	(2.51) 2.29	(1.50) 1.35	0.0 (all)	1.0	(0) 80	Large Spherical
Mineral Dust [†] (Accum.)	0.05	2.0	0.47	2.60	1.53	0.0085(1) 0.0055(2) 0.0045(3) 0.0012(4)	0.91	--	Medium Non-spherical
Mineral Dust [†] (Coarse)	0.5	15.0	1.90	2.60	1.53	0.0085(1) 0.0055(2) 0.0045(3) 0.0012(4)	0.73	--	Large Non-spherical
Carbonaceous ^{††}	0.007	2.0	0.13	1.80	1.50	0.025 (all)	0.87	97	Medium Spherical
Black Carbon	0.001	0.5	0.012	2.00	1.75	0.455(1) 0.440(2) 0.435(3) 0.430(4)	0.17	--	Small
Thin Cirrus ^{††}	3.0	200.	--	--	1.316(1) 1.311(2) 1.308(3) 1.304(4)	0.0 (all)	1.0	100	Very large Fractal

*This table is taken from Table 3 of *Kahn et al.* [1999]. r_1 and r_2 are the lower and upper radius limits for the particle size distribution. "Accum." stands for "accumulation mode" particles. Particle types are distributed log-normally, with characteristic radius r_c and width σ . ω_0 is the single scattering albedo, given here at the effective wavelength of the MISR red channel. RH is the relative humidity to which hygroscopic particles are hydrated. Sulfate and sea salt particles are hydrated to the RH value in the "RH" column using the model of *Hanel* [1976]; where properties for these particle types are in parentheses, they refer to the dry particles. The aerosol physical data are abstracted from *Shettle and Fenn* [1979], *d'Almeida et al.* [1991], *WCP* [1984], and other sources, except as indicated. Optical data for spherical particles are calculated using standard Mie theory.

[†] Non-spherical (mixed spheroid) mineral dust models based on *Mishchenko et al.* [1997].

^{††} Carbonaceous particle model based on *Reid et al.* [1998].

^{††} Fractal thin cirrus model based on *Mishchenko et al.* [1996].

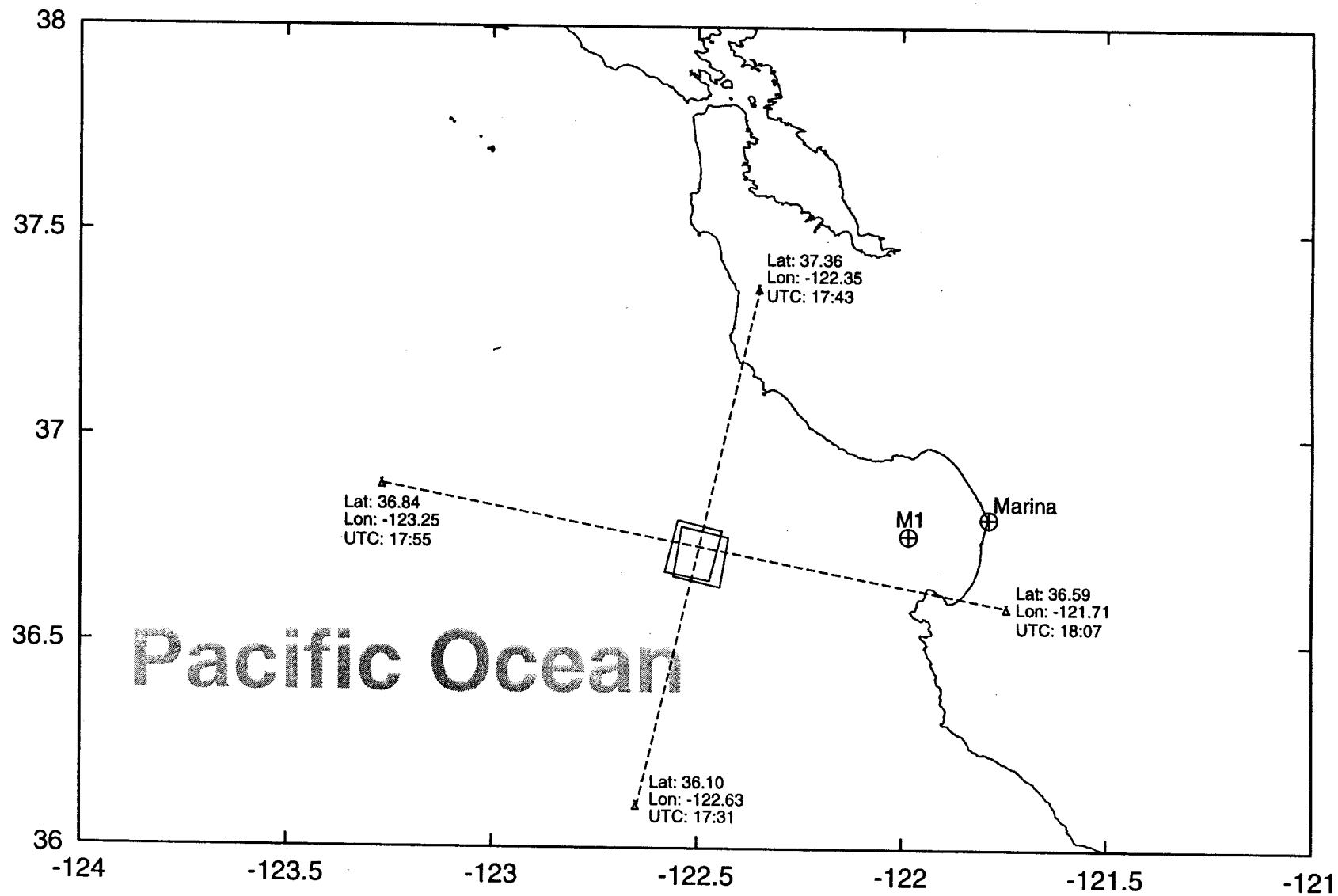


Fig. 1

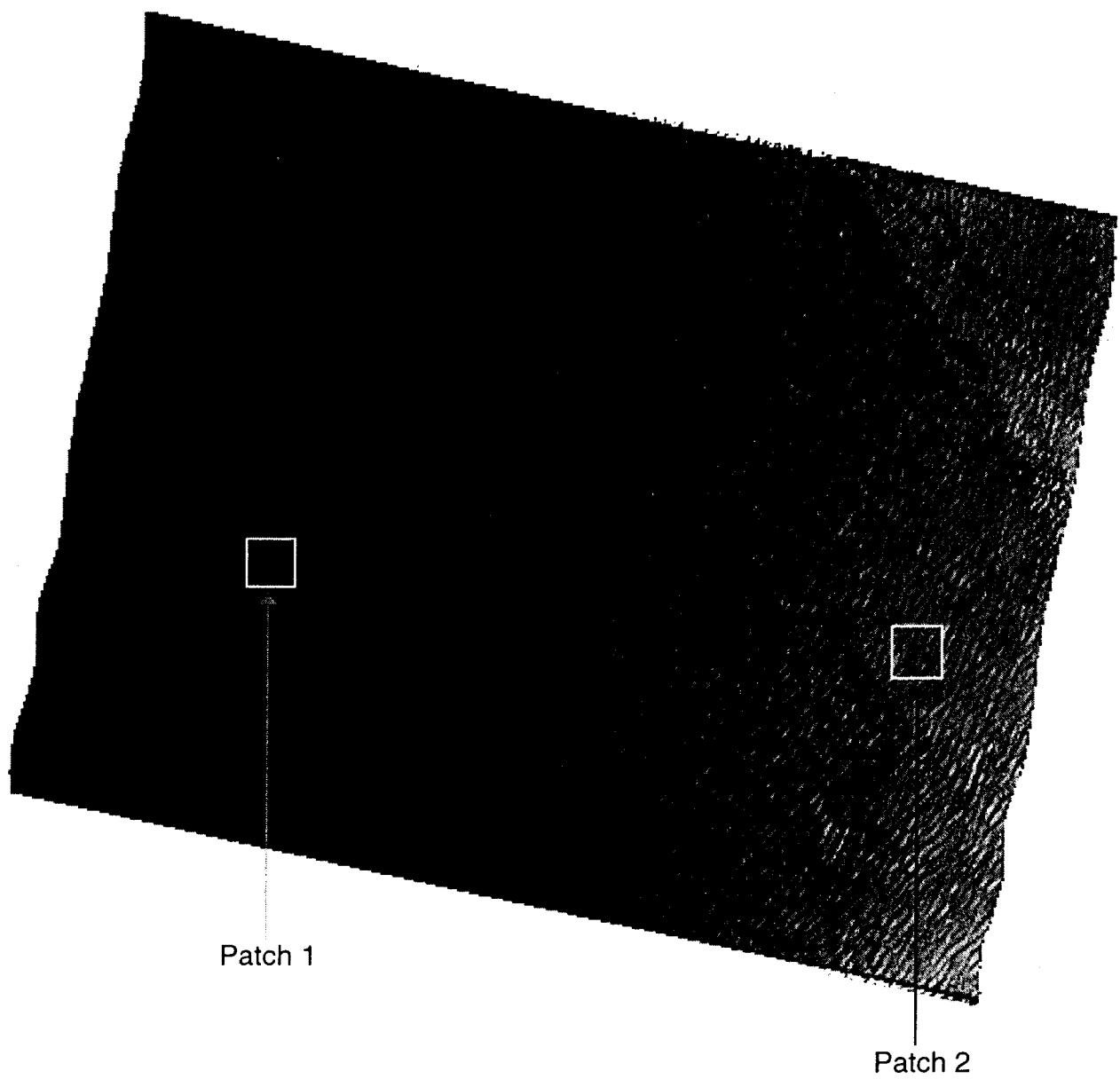
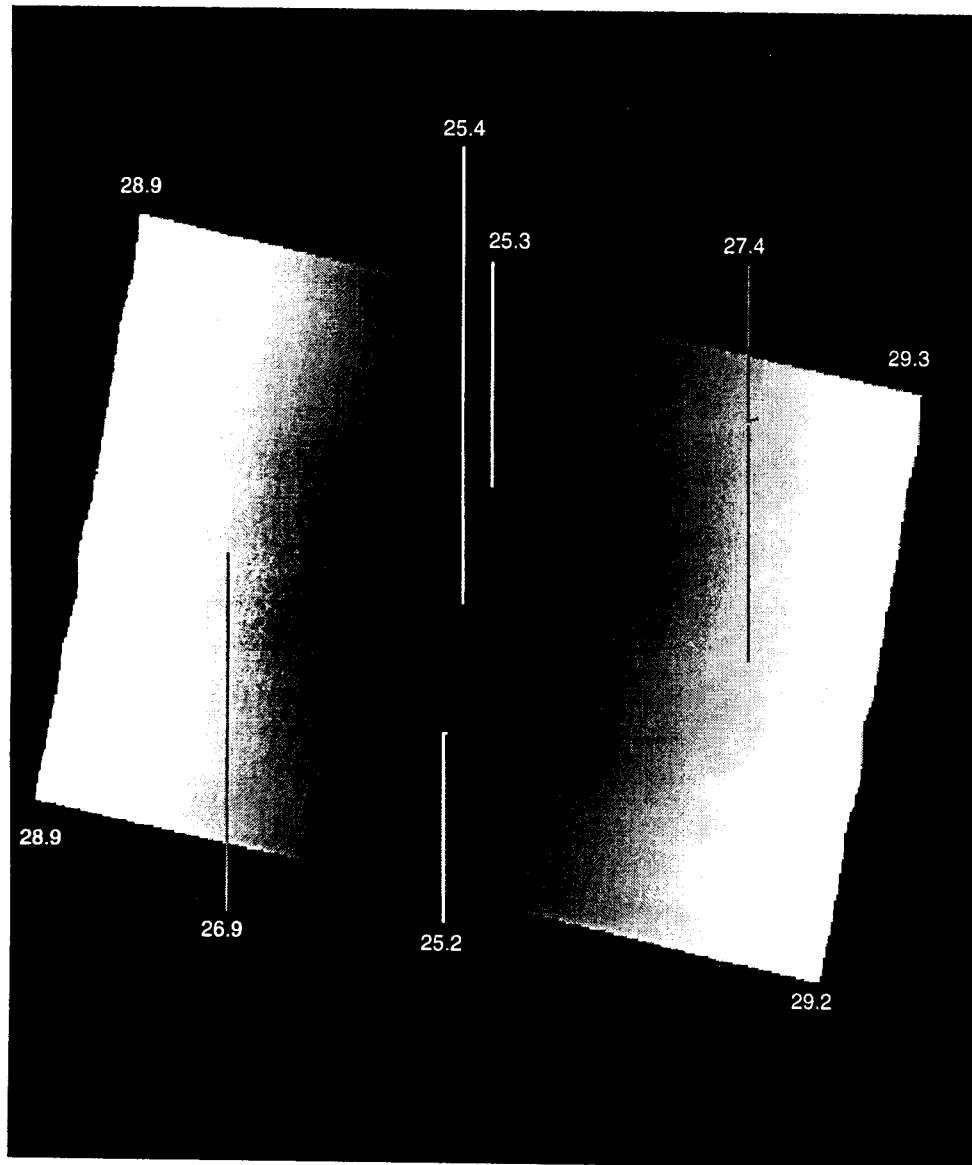
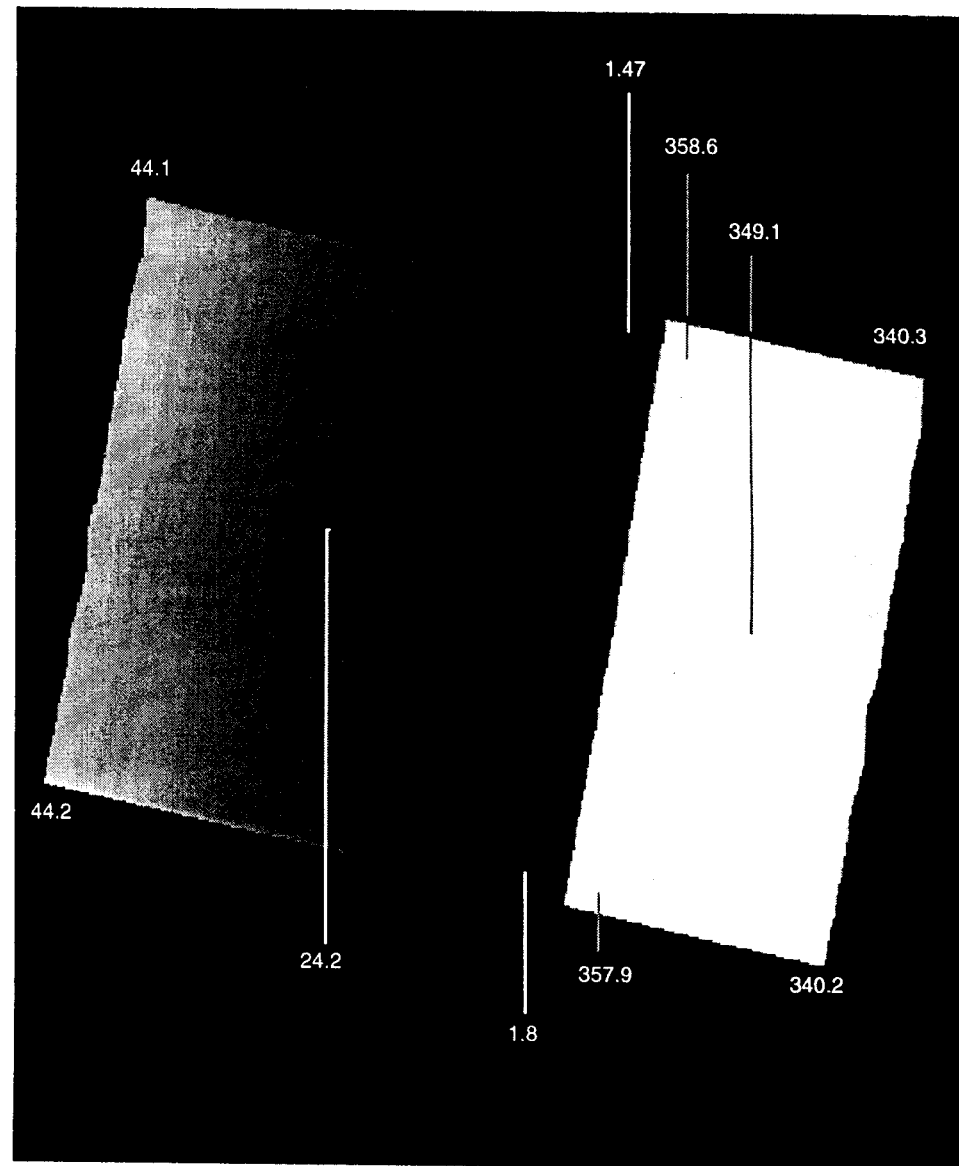


Fig. 2



(a)



(b)

Fig. 3

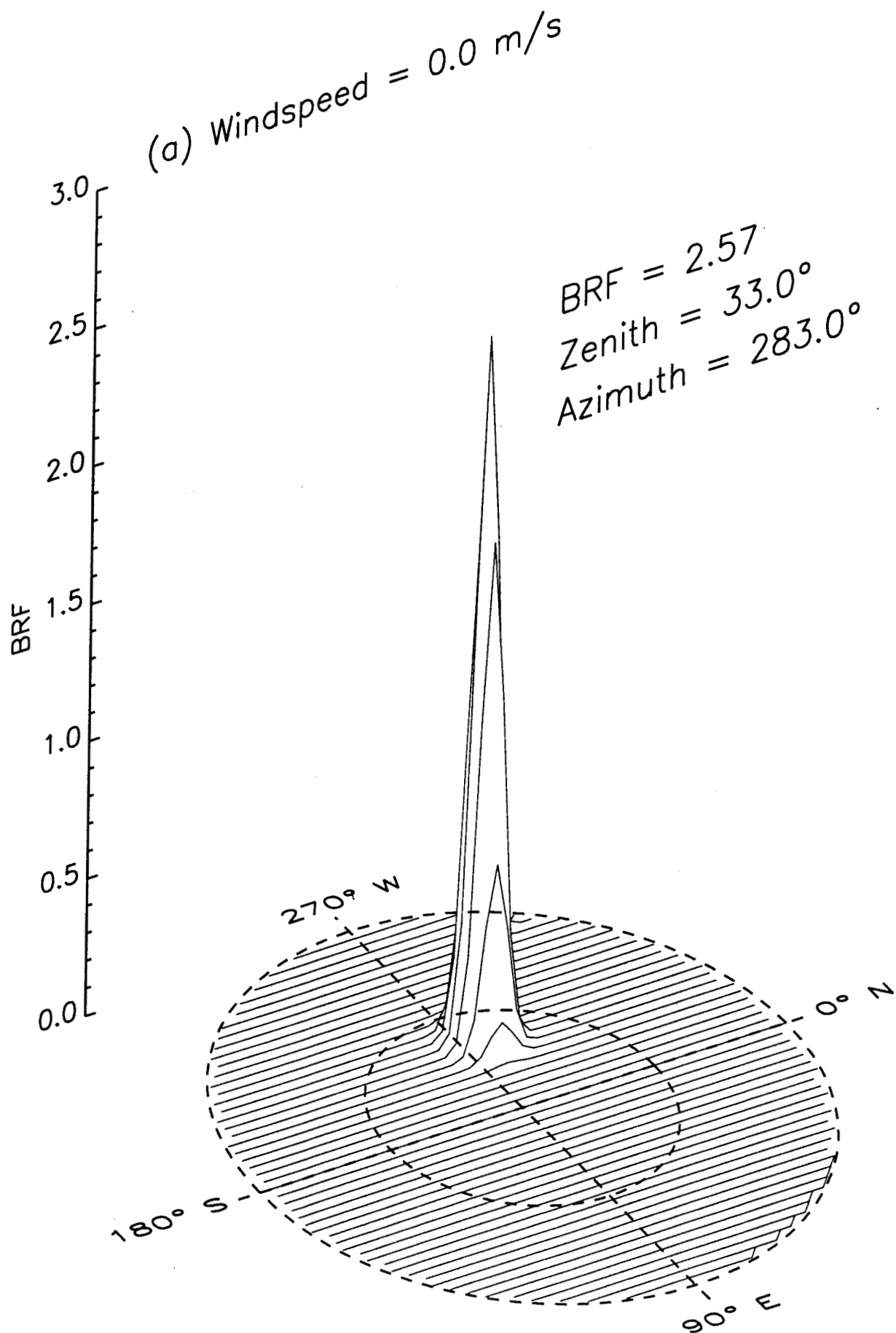


Figure 4c

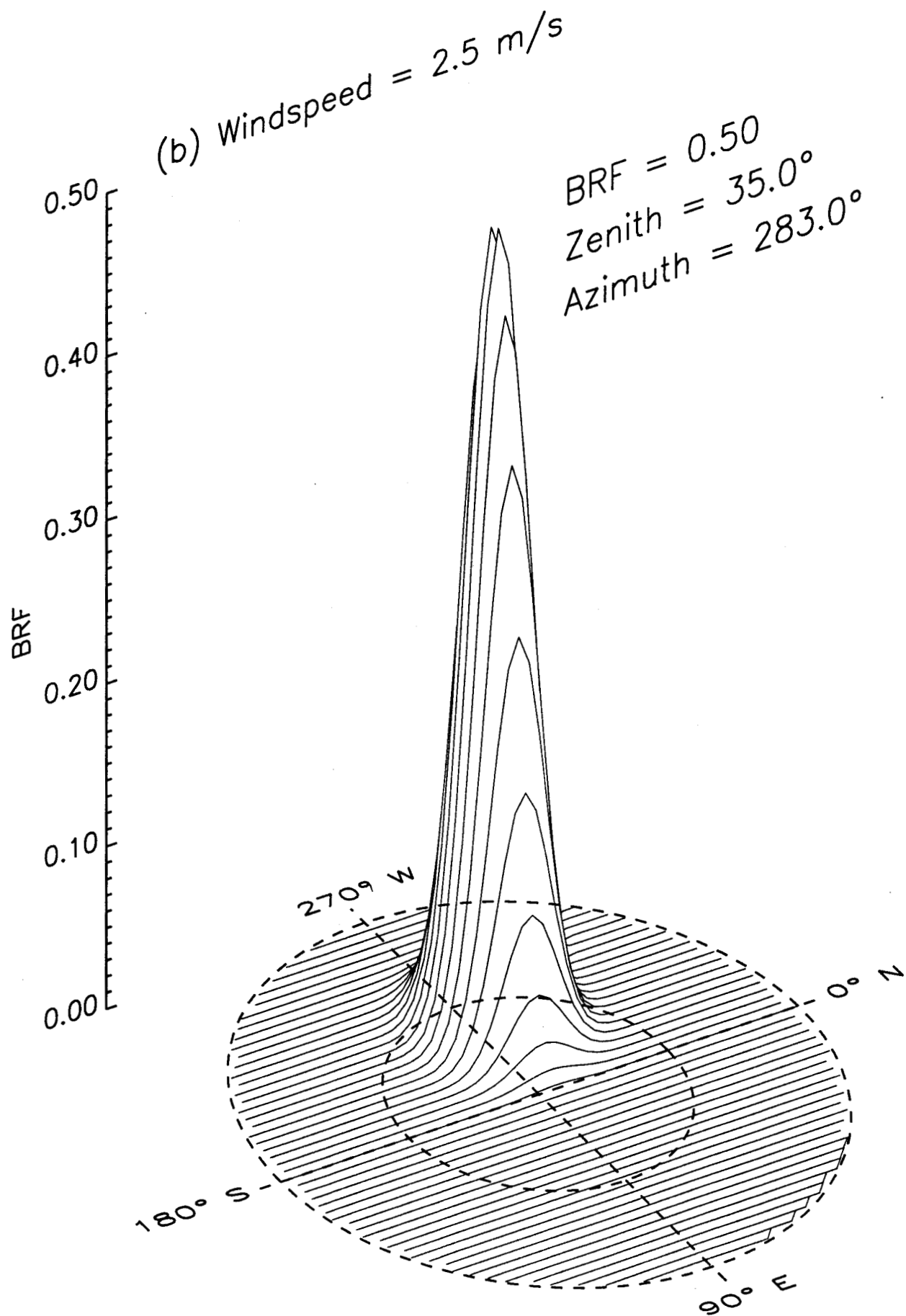


Figure 4b

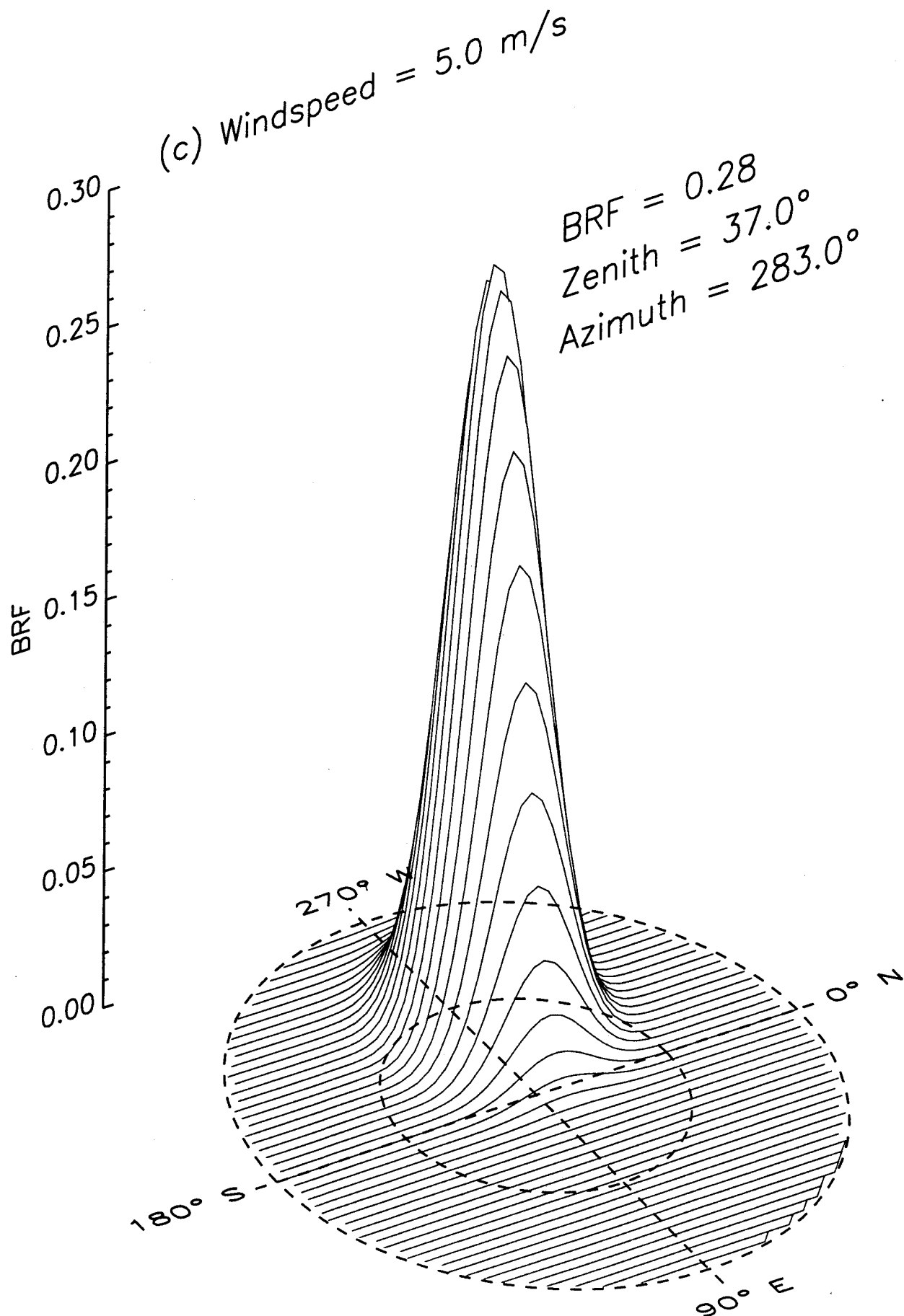


Figure 4c

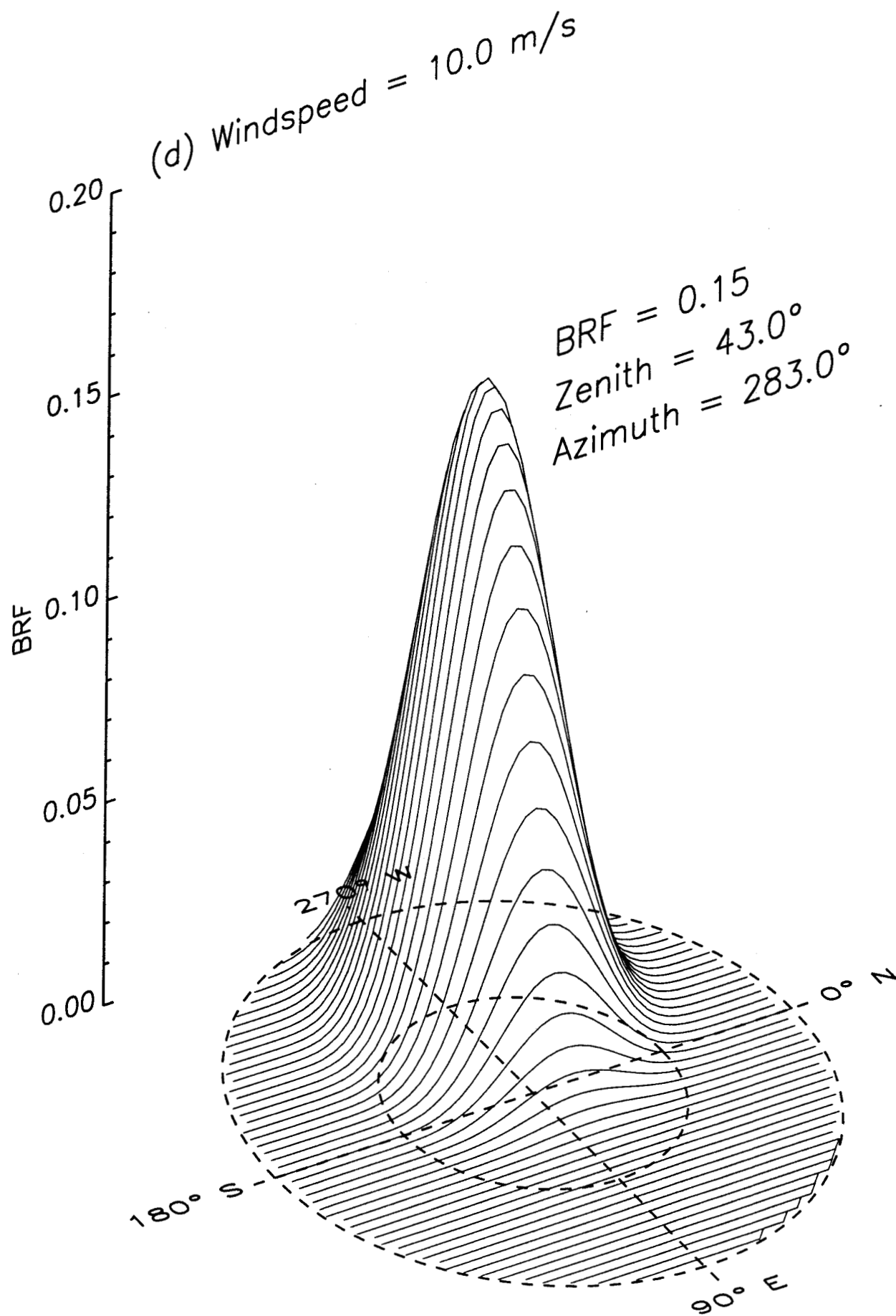
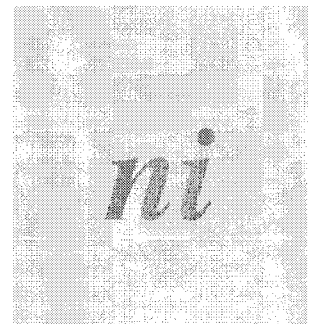
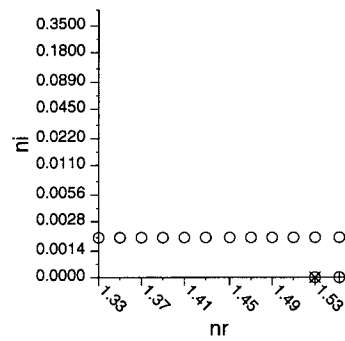
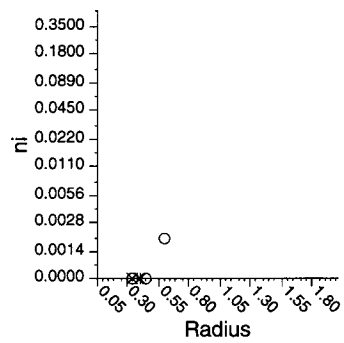
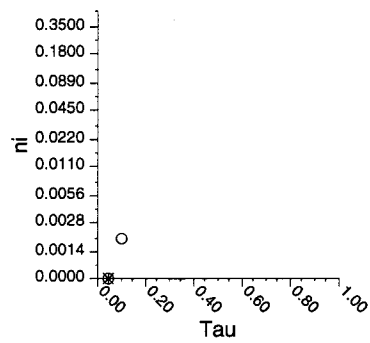
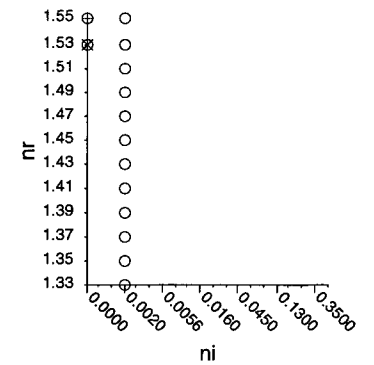
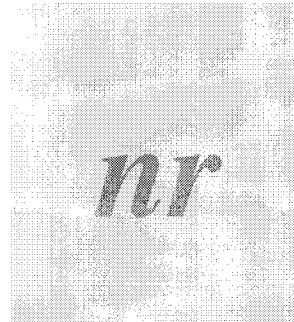
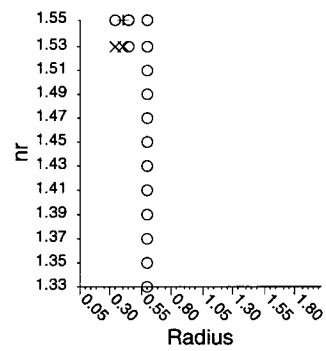
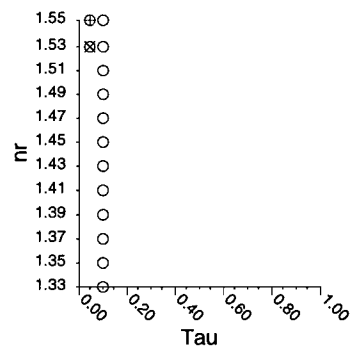
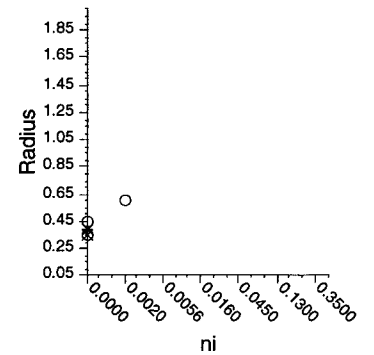
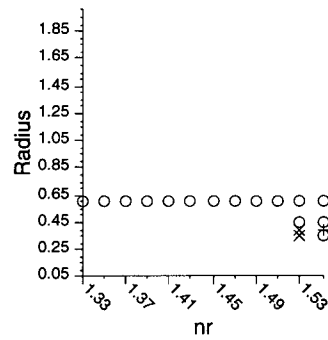
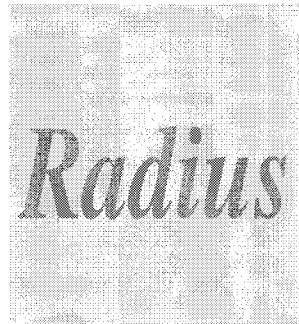
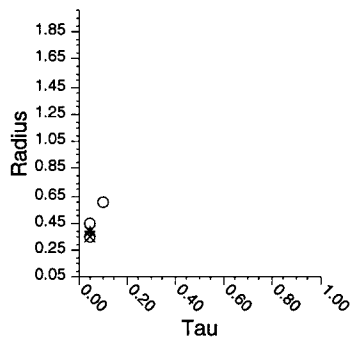
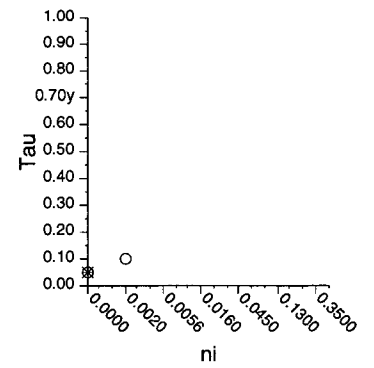
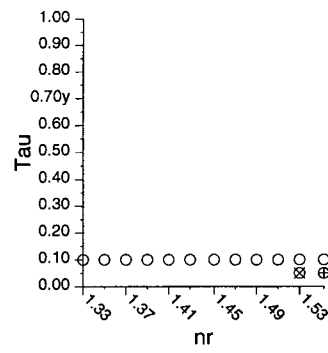
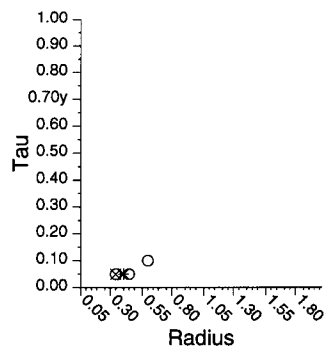
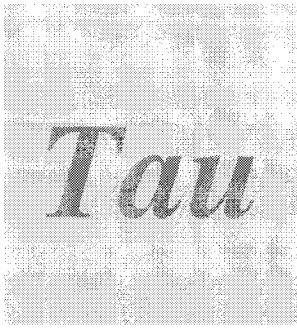


Figure 4c

atm_stats index = 0, windspeed index = 1



- × $\text{chisq} < 17.5$
- + $17.5 \leq \text{chisq} < 20.0$
- $20.0 \leq \text{chisq} < 22.5$

- △ $22.5 \leq \text{chisq} < 25.0$
- $25.0 \leq \text{chisq} < 27.5$

